

# Searches for Shapiro delay in seven binary pulsars using the MeerKAT telescope

M. Shamohammadi,<sup>1,2\*</sup> M. Bailes,<sup>1,2</sup> P. C. C. Freire,<sup>3</sup> A. Parthasarathy,<sup>3</sup> D. J. Reardon,<sup>1,2</sup> R. M. Shannon,<sup>1,2</sup> V. Venkatraman Krishnan,<sup>3</sup> M. C. i. Bernadich,<sup>3</sup> A. D. Cameron,<sup>1,2</sup> D. J. Champion,<sup>3</sup> A. Corongiu,<sup>5</sup> C. Flynn,<sup>1,2</sup> M. Geyer,<sup>6</sup> M. Kramer,<sup>3</sup> M. T. Miles,<sup>1,2</sup> A. Possenti,<sup>5</sup> R. Spiewak<sup>1,2,4</sup>

<sup>1</sup>Centre for Astrophysics and Supercomputing, Swinburne University of Technology, PO Box 218, Hawthorn, VIC 3122, Australia

<sup>2</sup>ARC Centre of Excellence for Gravitational Wave Discovery (OzGrav), Mail H29, Swinburne University of Technology, PO Box 218, Hawthorn, VIC 3122, Australia

<sup>3</sup>Max-Planck-Institut für Radioastronomie, Auf dem Hügel 69, D-53121 Bonn, Germany

<sup>4</sup>Jodrell Bank Centre for Astrophysics, Department of Physics and Astronomy, University of Manchester, Manchester M13 9PL, UK

<sup>5</sup>INAF–Osservatorio Astronomico di Cagliari, Via della Scienza 5, I-09047 Selargius (CA), Italy

<sup>6</sup>South African Radio Astronomy Observatory, 2 Fir Street, Black River Park, Observatory 7925, South Africa

Accepted XXX. Received YYY; in original form ZZZ

## ABSTRACT

Precision timing of millisecond pulsars in binary systems enables observers to detect the relativistic Shapiro delay induced by space time curvature. When favourably aligned, this enables constraints to be placed on the component masses and system orientation. Here we present the results of timing campaigns on seven binary millisecond pulsars observed with the 64-antenna MeerKAT radio telescope that show evidence of Shapiro delay: PSRs J0101–6422, J1101–6424, J1125–6014, J1514–4946, J1614–2230, J1732–5049, and J1909–3744. Evidence for Shapiro delay was found in all of the systems, and for three the orientations and data quality enabled strong constraints on their orbital inclinations and component masses. For PSRs J1125–6014, J1614–2230 and J1909–3744, we determined pulsar masses to be  $M_p = 1.68 \pm 0.17 M_\odot$ ,  $1.94 \pm 0.03 M_\odot$  and  $1.45 \pm 0.03 M_\odot$ , and companion masses to be  $M_c = 0.33 \pm 0.02 M_\odot$ ,  $0.495 \pm 0.005 M_\odot$  and  $0.205 \pm 0.003 M_\odot$ , respectively. This provides the first independent confirmation of PSR J1614–2230’s mass, one of the highest known. The Shapiro delays measured for PSRs J0101–6422, J1101–6424, J1514–4946, and J1732–5049 were only weak, and could not provide interesting component mass limits. Despite a large number of millisecond pulsars being routinely timed, relatively few have accurate masses via Shapiro delays. We use simulations to show that this is expected, and provide a formula for observers to assess how accurately a pulsar mass can be determined. We also discuss the observed correlation between pulsar companion masses and spin period, and the anti-correlation between recycled pulsar mass and their companion masses.

**Key words:** stars: neutron – pulsars: general – pulsars: individual – telescopes

## 1 INTRODUCTION

Radio pulsars are rapidly rotating neutron stars, with radio emission arriving at our observatories as a highly predictable train of pulses. The group of pulsars that have a spin period of  $P \leq 30$  ms and a rate of spin-down of  $\dot{P} \leq 10^{-17}$  are often called millisecond pulsars (MSPs). This subclass is thought to be produced through mass transfer from an evolving giant companion star (during the Roche-lobe overflow (RLO) stage) onto the neutron star. The consequent transfer of angular momentum during this stage decreases the spin period of the pulsar, reduces the magnetic field strength and circularises its orbit (Radhakrishnan & Srinivasan 1982; Alpar et al. 1982; Lorimer 2008; Tauris & van den Heuvel 2023).

Owing to their high rotational stability, MSPs have been used as astrophysical tools in Pulsar Timing Arrays (PTAs) to search for

ultra-low (nanohertz) frequency gravitational waves (Shannon et al. 2015; Hobbs & Dai 2017; Arzoumanian et al. 2020; Goncharov et al. 2021; Chalumeau et al. 2022; Antoniadis et al. 2022). In some binary pulsars, we can detect relativistic effects in the orbital motion and the propagation of light in the spacetime of the system, these are quantified by the so-called ‘post-Keplerian’ (PK) parameters.

With two PK parameters, we can use a theory of gravity to derive the masses of the pulsar and the companion object, as well as the orbital inclination angle with respect to our line of sight (Kiziltan et al. 2013; Özel & Freire 2016). Measuring pulsar masses helps us to determine the underlying distribution of neutron star masses (see also Antoniadis et al. 2016). The neutron stars with highest masses probe the Equation of State (EOS) of nuclear matter (Lattimer & Prakash 2004) (for instance PSR J1614–2230 Arzoumanian et al. 2018, PSR J0348+0432 Antoniadis et al. 2013 and PSR J0740+6620 Fonseca et al. 2021), since any EOS that fails to predict such massive

\* E-mail: msh.ph.ir@gmail.com

neutron stars can be ruled out (Lattimer & Prakash 2004; Özel & Freire 2016)<sup>1</sup>.

If we measure more than two PK parameters, we can test the theory of gravity being used to interpret them, by verifying whether each pair of PK parameters yields consistent mass estimates (Stairs 2003; Kramer et al. 2006; Kramer 2014; Krishnan 2019; Kramer et al. 2021a; Freire 2022). In some extreme cases, we can even look for other relativistic effects like spin-orbit coupling (Weisberg et al. 1989; Stairs et al. 2004; Fonseca et al. 2014; Venkatraman Krishnan et al. 2020), which might, in some cases, provide additional tests of GR and even constrain the neutron star EOS (Hu et al. 2020).

In pulsar timing, it is a standard practice to develop a timing model via an iterative procedure that can accurately predict the time of arrival of every pulse (ToA). The timing model includes parameters that describe the pulsar's spin, astrometric, and orbital properties; however, there are also noise processes that can be correlated with parameters in the timing model. The timing model is then iteratively updated using software such as TEMPO2 (Hobbs et al. 2006; Edwards et al. 2006), which is used to calculate and analyse timing residuals. To properly analyse the arrival times, we need to account for the noise processes, which for the purposes of this analysis, are limited to the systematic white noise, achromatic red noise, and that induced by dispersion measure variations.

According to the general theory of relativity, the Shapiro delay is the additional delay in the propagation of any signal travelling at the speed of light caused by the space-time curvature near massive objects (Shapiro 1964). If a pulsar's orbit is observed close to edge-on, the Shapiro delay caused by the space-time curvature near the companion can be detected in the pulsar signal; in such cases it can be used to constrain the component masses and system's orbital inclination. The shape of the timing residuals as a function of orbital phase determines the orientation, and the amplitude of the delay peak is proportional to the companion mass.

In this paper, we present timing and noise analyses of seven binary MSPs: PSR J0101–6422, J1101–6424, J1125–6014, J1514–4946, J1614–2230, J1732–5049, and J1909–3744, using observations from the 64-antenna MeerKAT radio telescope.

Among these MSPs, PSRs J1909–3744 and J1614–2230 are of great importance. PSR J1909–3744 has an extremely narrow pulse (Jacoby et al. 2003). For that reason, it has the highest timing precision of any pulsars known (Miles et al. 2022). This, in combination with the high orbital inclination resulted in the first precise mass measurement for an MSP (Jacoby et al. 2005). The high timing precision means it has been timed by all the major timing arrays (Shannon et al. 2013; Lentati et al. 2015; Arzoumanian et al. 2020); this has resulted in multiple independent measurements of its mass (Arzoumanian et al. 2018; Liu et al. 2020; Reardon et al. 2021).

For more than a decade, PSR J1614–2230 has been one of the most important pulsars for constraining EOSs due to its high mass. Demorest et al. (2010) found the mass of the pulsar to be  $1.97 \pm 0.04 M_{\odot}$  by measuring the amplitude of the Shapiro time delay with the Green Bank Telescope. This mass has been refined since (Fonseca et al. 2016; Arzoumanian et al. 2018), but these masses have never been confirmed with data from other radio telescopes.

The MeerTime Pulsar Timing Array (MPTA) has been established to frequently observe up to 89 pulsars with extremely high preci-

sion (Miles et al. 2022) with the aims of searching for gravitational waves coming from merging supermassive black hole binaries, testing theories of gravity, studying the structure of interstellar plasma, exploring the interior structure of neutron stars, and understanding the origin and evolution of MSP binary systems<sup>2</sup>. By augmenting the MPTA data set with intense observing campaigns around superior conjunction, the ongoing Relativistic Binary programme (Kramer et al. 2021b) under the MeerTime Large Survey Project with the MeerKAT telescope (Bailes et al. 2020) is aiming to increase the number of known pulsar masses amongst other objectives (e.g. Serylak et al. (2022)). This paper, as a part of the Relativistic Binary programme, investigates measurements of Shapiro delay and (where possible) the derived masses of seven MSPs and their companion stars. In Section 2, we describe the MeerKAT observations and the data processing leading to the calculation of the ToAs. In Section 3, we present our methods for modelling noise processes, updating the timing models, and measuring the Shapiro delays. In Section 4, we present our results on constrained masses and orbital inclination angles. We also present two simulations performed for exploring the change in the pulsar mass error as a function of the orbital inclination angle. In Section 5, we discuss our measurements and compare them to previous values, finding good agreement and explore correlations between the component masses and the spin periods of recycled pulsars. In Section 6, we summarise the major results and draw our conclusions.

## 2 THE DATA SET

The observations of the MSP sample began in early 2019 and concluded in early 2022. Observations were also conducted as part of the MeerTime Pulsar Timing Array project (Miles et al. 2022, in press). The observations were performed with the 64-dish MeerKAT radio telescope using two receivers: the Ultra-High Frequency (UHF) receiver, operating between 544–1088 MHz, and the L-band receiver, operating between 856–1712 MHz, both with 1024 frequency channels (Bailes et al. 2020). Using the two receivers, we collected coherently de-dispersed data folded in real time at the apparent pulsar period; at each observing session only one receiver was used. PSRs J1101–6424, J1125–6014, J1514–4946, J1614–2230, and J1909–3744 have been observed with the L-band receiver only. UHF observations of PSR J0101–6422 and J1732–5049 were included as these had relatively steep spectral indices of  $-1.7$  and  $-1.9$ , respectively, (Gitika et al. in prep) and benefitted from UHF observing campaigns near superior conjunction. The minimum number of 37 observations was for PSR J1514–4946 and the maximum number of 187 observations was for J1909–3744, over a three year time span, and have good orbital coverage. For each pulsar, we conducted a long, targeted observing campaign, centred in time near superior conjunction (where the companion passes between the Earth and the pulsar), to optimise our sensitivity to the Shapiro delay. A summary of the data spans, total integration times, and the number of observations for each pulsar are listed in Tables A1 and A2.

Frequency channels affected with radio-frequency interference (RFI) were zero-weighted with the `RFIHUNTER` RFI rejection tool<sup>3</sup>. This software subtracts a normalised and phase-aligned mean pulse profile from the data and creates pulse profile residuals. To do this, it fits a smoothed integrated pulse profile to each 8-sec integrated

<sup>1</sup> We note that even more massive neutron stars could exist (e.g., Romani et al. 2021, 2022), but such masses were not obtained from the measurement of PK parameters, and rely on assumptions about surface heating and reradiation and are more model-dependent as a result.

<sup>2</sup> [www.meertime.org](http://www.meertime.org)

<sup>3</sup> <https://github.com/mshamohammadi/rfihunter>

frequency channel, using a non-linear least squares fitting algorithm. The pulse residuals are then searched for the detection of RFI-affected frequency channels, after normalising with a ‘median bandpass model’. Following this, the frequency channels with statistics above  $3.5\sigma$  from the median are zero-weighted, similar to the method that was employed in Bailes et al. (2020). The statistics used for RFI excision are 1) the maximum amplitude of the Fourier transform of the mean-subtracted residuals, 2) the standard deviation, and 3) the range (following the statistics used in Lazarus et al. (2016)). To construct a median bandpass model of each receiver, we used the off-pulse baselines and used the Gaussian Process Regression module<sup>4</sup> implemented in SCIKIT-LEARN package (Pedregosa et al. 2011) to determine a robust median.

After RFI excision, we installed pulsar ephemerides updated for the work of Spiewak et al. (2022, private communication), averaged the observations in time and reduced the data to 16 frequency channels. This channelisation allowed us to take into account the temporal variations of pulsar dispersion-measure (DM) (Keith et al. 2013; Jones et al. 2017), as well as the detection of the in-band profile evolution, which requires frequency-dependent parameters in our timing solution (Demorest et al. 2013).

For every pulsar, we summed high signal-to-noise observations in time, polarization, and frequency, and then using wavelet smoothing techniques implemented in the PSRCHIVE program `psrsmooth`, we created a noise-free pulse profile, often termed a ‘standard’ or ‘template’. For PSRs J1614–2230 and J1909–3744, we used Pulse-Portraiture<sup>5</sup> to create a frequency-dependent template, which is a profile that evolves in frequency, referred to as a ‘portrait’ (Pennucci 2019), the aim of which is to account for frequency-dependent time delays caused by profile evolution. This was possible because we had very high signal-to-noise ratio observations of these two pulsars, making the profile evolution with frequency secure.

Finally, we used the Fourier domain Monte Carlo (FDM) algorithm in `pat`, which fits for a phase gradient between the Fourier transforms of the template and profile, to calculate a ToA for every pulse profile, and selected the profiles with a signal-to-noise ratio higher than 10. This algorithm uses a Markov Chain Monte Carlo method to determine the likely ToA uncertainties.<sup>6</sup>

### 3 METHODS

For standard pulsar timing practices, we need a timing model (solution) that includes pulsar parameters such as its astrometry, spin, dispersion measure, binary motion (five Keplerian parameters), and a Solar System model. The astrometric parameters include position (Right Ascension  $\alpha$  and Declination  $\delta$ ), proper motion ( $\mu_\alpha \cos \delta$ ,  $\mu_\delta$ ), and when significant, a parallax. When profiles possess strong profile evolution as a function of frequency, radio frequency derivative parameters are added to the timing model. A list of systematic jumps are also added to the timing model if needed between frequency bands or observational set-ups. We commenced our timing with the latest pulsar ephemerides from Spiewak et al. (2022, private communication) as the initial timing models, and added two Shapiro parameters (will be discussed below) into the models, and refined these based upon our ToAs using TEMPO2, utilizing a generalized

least-squares fitting method to minimize the timing residuals, and updated them constantly by adding ToAs from new observations. We used JPL DE440 as our Solar System ephemeris (Park et al. 2021), the Bureau International des Poids et Mesures BIPM2020 as our realization of terrestrial time, and Barycentric Coordinate Time (TCB) for our units.

#### 3.1 Timing model

For a pulsar in a binary with a low eccentricity,  $e$ , it is difficult to measure the longitude of periastron,  $\omega$ , and there is a high correlation between the longitude of periastron and the time of periastron,  $T_0$ . In such systems, there is typically a high correlation between the orbital period,  $P_b$ , and the time-derivative of the longitude of periastron,  $\dot{\omega}$ . The ELL1 binary model can address this problem in systems with a low  $e$  (Lange et al. 2001). Instead of  $e$ ,  $\omega$ , and  $T_0$ , this model uses the time of passage through the ascending node,  $T_{\text{asc}}$ , and the two Laplace-Lagrange parameters,  $\eta \equiv e \sin \omega$  and  $\kappa \equiv e \cos \omega$ , which can be measured with less covariance.

The effects of Shapiro delay have been parameterised in two binary models implemented in TEMPO2: DD (Damour & Deruelle 1986) and ELL1 using a function of two post-Keplerian (PK) parameters: range ( $r$ ) and shape ( $s$ ) in the following forms:

$$r = T_\odot M_c \quad (1)$$

$$s = \sin i \quad (2)$$

where  $M_c$  is the mass of the companion and  $T_\odot \equiv G M_\odot c^{-3} = 4.925490947 \mu\text{s}$  is the mass of the Sun in time units. The Shapiro delay,  $\Delta_s$ , in the ELL1 binary model is modelled as

$$\Delta_s = -2r \ln(1 - s \sin \Phi), \quad (3)$$

where  $\Phi$  is the celestial longitude of the binary. At high inclination angles, where  $\sin i \sim 1$ , the peak of the Shapiro delay is very pronounced, but at other inclinations it becomes extremely covariant with the Römer delay (caused by the pulsar’s orbital motion, Lange et al. 2001) from the circular orbit.

The problem with  $r$  and  $s$  is that they become highly correlated, in particular at low (i.e. face-on) orbital inclinations. Because of this, Freire & Wex (2010) parameterised the Shapiro delay for low-eccentric binary pulsars in Fourier space, using the sum of the harmonics of the Shapiro delay. They introduced the two new PK parameters that are proportional to the third and fourth harmonic amplitudes ( $h_3, h_4$ ). For higher inclinations, the best parameterisation is  $h_3$  and  $\varsigma = h_4/h_3$ , because the latter parameter can be measured more precisely than  $h_4$ . The main advantage of these ‘orthometric’ parameters is that they are less correlated with one another compared to  $r$  and  $s$ , thus providing an optimal description of the  $m_c, \sin i$  constraints provided by the Shapiro delay. The orthometric parameters relate to  $r, s$  according to the following relations (Freire & Wex 2010):

$$\varsigma = \frac{s}{1 + \sqrt{1 - s^2}} \quad (4)$$

$$h_3 = r \varsigma^3, \quad (5)$$

and obtained the equivalent Shapiro delay formula

$$\Delta_s = -\frac{2h_3}{\varsigma^3} \ln(1 + \varsigma^2 - 2\varsigma \sin \Phi). \quad (6)$$

Within the range of possible orbital inclinations ( $0^\circ \leq i \leq 180^\circ$ ), we have  $0 \leq \sin i \leq 1$ ; this implies that  $0 \leq \varsigma \leq 1$  and  $h_3 > 0$  (since  $r \equiv T_\odot M_c$  must be positive).

Three new binary models were established based upon the ( $h_3, h_4$ )

<sup>4</sup> [https://scikit-learn.org/stable/modules/gaussian\\_process.html](https://scikit-learn.org/stable/modules/gaussian_process.html)

<sup>5</sup> <https://github.com/pennucci/PulsePortraiture/tree/py3>

<sup>6</sup> The algorithm is in the ProfileShiftFit.C source code from the psrchive sourceforge.net repository.

and  $(h_3, \varsigma)$  parameterisations and implemented in the ELL1H binary model as an alternative to the ELL1 binary model. In this work, we have used these models with the  $h_3$  and  $\varsigma$  parameterisation when searching for the relativistic Shapiro delay in the timing residuals for each pulsar because the binaries being studied have relatively high orbital inclinations. We note that, although physical constraints require that  $0 \leq \varsigma \leq 1$  and  $h_3 > 0$ , such constraints are not enforced by the ELL1H orbital model, in the same way that the conditions  $0 \leq s \leq 1$  and  $r > 0$  are not enforced by any orbital model when fitting for  $r$  and  $s$ .

### 3.2 Noise models

There are two basic contributions in calculating timing residuals; the deterministic and stochastic noise components (Lentati et al. 2014). The latter can be modelled using three white and two red stochastic processes:

(i) White (time uncorrelated) noise: can be described using three components as follows:

(a) EFAC: a factor  $\alpha_i$  that is multiplied to any ToA uncertainty  $\sigma_i$ , where  $i$  is the  $i$ -th ToA. One possible contribution to this term is due to the radiometer noise after measuring ToA uncertainty using the template matching algorithm. For every receiver, backend, or pulsar, we might need to use different EFAC parameter.

(b) EQUAD: an error term  $\beta_i$  that is added in quadrature to the scaled ToA uncertainty by EFAC. It is usually necessary to have separate EQUAD parameters for different receiver, backend, or pulsar. Therefore, the uncertainty of the  $i$ -th ToA scaled with EFAC and EQUAD can be written as

$$\sigma_{i, \text{whitened}}^2 = (\alpha_i \sigma_i)^2 + \beta_i^2. \quad (7)$$

(c) ECORR: a noise term that describes the correlations between the sub-bands of one observation, and is not correlated between observations taken at different epochs. We used the TECORR parameter described in Equation 1 in Bailes et al. (2020) in our noise analysis.

(ii) Red noise: This term accounts an achromatic stationary Gaussian process with a low-frequency, and is modeled using a power-law spectrum that has a form of

$$P_{\text{red}}(f) = A_{\text{red}}^2 \left( \frac{f}{1 \text{ yr}^{-1}} \right)^{\gamma_{\text{red}}} \quad (8)$$

where  $S_{\text{red}}(f)$  is the red noise power spectral density at frequency  $f$ .  $A_{\text{red}}$  is the amplitude of the red noise in  $\mu\text{s yr}^{1/2}$ , and  $\gamma_{\text{red}}$  is the spectral index of the noise process.

(iii) Dispersion noise: pulses at higher frequencies arrive earlier in a dispersive interstellar medium (ISM). The delay due to the frequency dispersion is measured (in seconds) using  $1/2.41 \times 10^{-4} \text{ DM}/\nu^2$ , where DM is the dispersion measure and  $\nu$  is the observing frequency in MHz. DM, measured in  $\text{pc cm}^{-3}$ , is the integral of the electron number density along our line of sight

$$\text{DM} = \int_0^L n_e(z) dz, \quad (9)$$

where  $L$  is the distance to the pulsar. Our line of sight changes due to the motion of the pulsar and the Earth, causing changes in the DM with time. Additionally, the turbulent ISM between the pulsar and the Earth has a bulk motion, which induces additional changes in the DM with time. Therefore, DM is epoch dependent, and DM

corrections are required after every observation. Through the use of broad band observations, it is possible to mitigate the effects of dispersion measure variations.

These temporal DM variation introduces an additional noise term in the timing residuals. We describe this temporal variation using a power-law spectrum that has a form similar to the red noise spectrum,

$$P_{\text{DM}}(f) = A_{\text{DM}}^2 \left( \frac{f}{1 \text{ yr}^{-1}} \right)^{\gamma_{\text{DM}}} \left( \frac{\nu}{\nu_c} \right)^{-2}, \quad (10)$$

where  $A_{\text{DM}}$  is the DM noise amplitude that scales with  $\nu^{-2}$ , and  $\nu_c$  is the centre frequency of the observation.

### 3.3 Noise analysis

We perform our noise analysis with TEMPONEST (Lentati et al. 2014), utilising an efficient Bayesian inference sampler, Multinest (Feroz & Hobson 2008; Feroz et al. 2009), for exploring the parameter space and producing marginal posterior distributions of parameters. Model comparison between two timing models can be quantified using the ratio of their evidences, which is called the Bayes factor  $\mathcal{B}$ . Using the evidences returned by TEMPONEST, we calculate the log Bayes factor,  $\ln \mathcal{B}$ , and define significant support for one model in comparison to another model as  $\mathcal{B} \geq 10$  (Kass & Raftery 1995), or  $\ln \mathcal{B} \geq 2.3$ .

### 3.4 Relativistic parameter derivations

There are additional physical parameters that can be derived from the measured parameters in the pulsar ephemerides. We can constrain the pulsar mass,  $M_p$ , the companion mass,  $M_c$ , and the orbital inclination angle,  $i$ , by measuring the relativistic Shapiro delay parameters,  $h_3$  and  $\varsigma$ , in our timing residuals. Every binary system has a precise binary mass function,  $f_m$ :

$$f_m = \frac{(M_c \sin i)^3}{(M_p + M_c)^2} = \frac{4\pi^2}{G} \frac{(a_p \sin i)^3}{P_b^2} = \frac{4\pi^2}{T_\odot} \frac{x^3}{P_b^2}, \quad (11)$$

which relates the unknown masses and the orbital inclination angle of the system. The mass function can be calculated using the observed orbital period and the observed projected semi-major axis of the pulsar,  $x = a_p \sin i/c$  in units of light-seconds, where  $a_p$  is the semi-major axis of the pulsar, and  $c$  is the speed of light. The quantity  $x$  can also experience a secular change, and it can experience a periodic modulation due to the orbital motion of the Earth around the Sun. This annual motion of the Earth causes the observed orbital inclination angle to have an annual periodic change that can be obtained by measuring the annual orbital parallax. In the case of the apparent change in  $x$  due to the proper motion, from Kopeikin (1996), the maximum value of  $\dot{x}/x$  provides an upper limit of

$$i \leq \tan^{-1} \left[ 1.54 \times 10^{-16} \left( \frac{\mu_T}{\text{mas yr}^{-1}} \right) / \left( \frac{\dot{x}}{x} \right)_{\text{max}} \right] \quad (12)$$

for the orbital inclination angle, where  $\mu_T$  is the total proper motion of the system in  $\text{mas yr}^{-1}$ . This provides another way to constrain the system inclination angle using the  $\dot{x}$  measurement.

In order to constrain the pulsar mass through the measurement of the Shapiro delay, it is necessary to constrain both the companion mass and the system inclination angle. So, the error in the pulsar mass  $\sigma_{M_p}$ , depends on the errors in both the companion mass  $\sigma_{M_c}$



and the sine of the inclination angle  $\sigma_{\sin i}$ , and can be estimated using partial derivatives of the mass function (Eq. 11),

$$\sigma_{M_p} \approx \sqrt{A^2 \sigma_{M_c}^2 + B^2 \sigma_{\sin i}^2 + 2AB \text{Cov}[M_c, \sin i]} \quad (13)$$

where

$$A = \frac{3M_c^{1/2} \sin i^{3/2}}{2f_m^{1/2}} - 1, \quad (14)$$

$$B = \frac{3M_c^{3/2} \sin i^{1/2}}{2f_m^{1/2}}, \quad (15)$$

and  $\text{Cov}[M_c, \sin i]$  is the covariance between  $M_c$  and  $\sin i$ . We note that this equation was used for an efficient estimate of the uncertainties of  $M_p$  in the simulations, not to estimate the uncertainties of  $M_p$  for the pulsars in his work.

## 4 RESULTS

A summary of spin, astrometric, orbital, and noise parameters for each pulsar is listed in the Tables A1 and A2 in Appendix A. For PSRs J1125–6014, J1614–2230 and J1909–3744, we report measurements of orthometric Shapiro parameters of  $h_3$  and  $\varsigma$ , and from these we have derived pulsar masses, the companion masses, and the orbital inclination angles. Figures C1, C2, and C3 provide the two-dimensional posteriors of the measured and the derived parameters. Among the seven pulsars, we have significantly measured the pulsar and the companion star masses for PSR J1125–6014, J1614–2230, and J1909–3744. These are described in section 4.1 and summarised in the Table 1. Considering the posterior probability distributions of the derived parameters, the values and their uncertainties are taken from the cumulative distribution function at the values of 0.16 (lower bound), 0.5 (median), and 0.84 (upper bound). We define the orbital inclination angles of the MSP binary systems to be in the range of  $0^\circ < i < 180^\circ$ . This definition satisfies the standard astronomical convention. In this work, we only report the solutions for the inclinations that are between  $0^\circ$  and  $90^\circ$ , corresponding to face-on and edge-on systems, respectively. However, there are another equally likely solutions of  $180 - i$ . We also quantify how the error in pulsar mass scales with  $\cos i$  using simulated ToAs in section 4.2, and explain why we were not able to measure the pulsar mass in the other four systems.

### 4.1 Measuring the Shapiro delay and constraining pulsar and companion masses

We saw significant evidence for Shapiro delay in all 7 systems, but could only accurately measure the pulsar masses in PSRs J1125–6014, J1614–2230 and J1909–3744. For PSRs J0101–6422, J1101–6424, J1514–4946, and J1732–5049, it was not possible for us to constrain the orthometric parameters significantly, as the uncertainties in the pulsar masses were greater than  $2M_\odot$ . Instead, for these systems, we assumed the pulsar mass to be greater than  $1.2M_\odot$  and for linearly spaced  $\cos i$  values from 0.01 to 0.99, with a resolution of 0.01, we calculated a series of  $(h_3, \varsigma)$  pairs. We then used every pair in the timing model and held them fixed while fitting for other parameters, and recorded a  $\chi^2$  value from TEMPO2. Afterwards, we differentiated the  $\chi^2$  values from the global minimum,  $\chi_{min}^2$ , to find a  $\Delta\chi^2$  value for every  $\cos i$ . Finally, we mapped them to a Bayesian likelihood function (Splaver et al.

2002), and calculated the  $1\sigma$  standard deviation of  $\cos i$ . This gave an estimate of the orbital inclination angle, and using the mass function formula (Eq. 11), we could find the  $1\sigma$  standard deviation of the companion mass. We repeated this analysis for a heavy pulsar mass of  $2.0M_\odot$  as well. Using the two, we could determine how likely the companion mass and the orbital inclination angle of the systems are, assuming the pulsar mass to be between  $1.2M_\odot$  and  $2.0M_\odot$ . We believe that the chosen values of  $1.2M_\odot$  and  $2.0M_\odot$  are justifiable as almost all known MSPs lie in this range, and we use this as a prior to explore what the companion masses and inclination angles are. These reported upper and lower limits of  $M_c$  and  $i$  are therefore reasonably conservative. Recently, it has been argued that PSR J0952–0607 has a pulsar mass of  $2.35 \pm 0.17M_\odot$  by examining its luminosity as a function of orbital phase and using its mass ratio from spectroscopic observations of the companion (Romani et al. 2022). If MSPs can be as massive as  $\sim 2.35M_\odot$  this would weaken these companion mass and inclination angle constraints but only mildly.

#### 4.1.1 PSR J0101–6422

PSR J0101–6422 is an MSP with a spin period of 2.57 ms in a 1.78 d orbit. It is an unidentified  $\gamma$ -ray source in the first *Fermi* Large Area Telescope catalog (Abdo et al. 2010), and was confirmed as an MSP with the Parkes radio telescope, also known as Murriyang, by Kerr et al. (2012). The results from the noise analysis showed that the model containing the white noise and the DM noise parameters had the highest Bayesian evidence. Comparing two timing models including one with the Shapiro parameters and one without, resulted in obtaining a log Bayes factor of  $\ln \mathcal{B} \sim 21$ , demonstrating that the model including the Shapiro parameters is preferred. We detected the Shapiro delay with  $\sim 4\sigma$  significance in  $h_3$  and  $\sim 8\sigma$  significance in  $\varsigma$ . Using the  $\chi^2$  analysis mentioned in 4.1, we place a constraint on  $\cos i$  to be in the range of  $0.24 \leq \cos i \leq 0.28$  if  $M_p = 1.2M_\odot$ , and  $0.29 \leq \cos i \leq 0.34$  if  $M_p = 2.0M_\odot$ . The corresponding companion mass and orbital inclination angle for the pulsar mass of  $M_p = 1.2M_\odot$  found to be in the ranges of  $0.14M_\odot \leq M_c \leq 0.16M_\odot$  and  $73^\circ \leq i \leq 75^\circ$ , and for the pulsar mass of  $M_p = 2.0M_\odot$  found to be in the ranges of  $0.20M_\odot \leq M_c \leq 0.22M_\odot$  and  $70^\circ \leq i \leq 74^\circ$ , respectively. These values are consistent with the predictions of Tauris & Savonije (1999) for a Helium white dwarf (He WD) star. Although these values are reasonably well bounded, they do not lead to interesting constraints on the pulsar’s mass.

#### 4.1.2 PSR J1101–6424

PSR J1101–6424 is an MSP with a spin period of 5.11 ms in a 9.61 d orbit. Ng et al. (2015) discovered the pulsar, during processing of the low-latitude Galactic plane data sets in the High Time Resolution Universe pulsar survey. Comparing the noise models, the model with the white noise and the DM noise parameters had the highest Bayesian evidence. We performed the noise analyses using two timing models with and without the Shapiro delay parameters, and obtained a log Bayes factor of  $\ln \mathcal{B} \sim 5$ . This indicates that we have a weak detection of Shapiro delay in our timing residuals. Using the  $\chi^2$  analysis mentioned in 4.1, we place a constraint on  $\cos i$  to be in the range of  $0.47 \leq \cos i \leq 0.60$  if  $M_p = 1.2M_\odot$ , and  $0.55 \leq \cos i \leq 0.67$  if  $M_p = 2.0M_\odot$ . The corresponding companion mass and orbital inclination angle for the pulsar mass of  $M_p = 1.2M_\odot$  found to be in the ranges of  $0.51M_\odot \leq M_c \leq 0.59M_\odot$  and  $53^\circ \leq i \leq 62^\circ$ , and for the pulsar mass of  $M_p = 2.0M_\odot$  found to be in the ranges of  $0.74M_\odot \leq M_c \leq 0.87M_\odot$  and  $47^\circ \leq i \leq 57^\circ$ ,

respectively. This is an interesting system, as the spin period (and even the orbital period) would suggest it is similar to J1614–2230, meaning that is possibly originated as Case A RLO (see discussion in section 5). The value of  $M_c$  might be consistent with that of J1614–2230.

#### 4.1.3 PSR J1125–6014

PSR J1125–6014 is a MSP with a spin period of 2.63 ms in a 8.75 d orbit. It is one of the 15 MSPs discovered by Faulkner et al. (2004) through a reprocessing of the Parkes Multibeam Pulsar Survey. The results from performing noise analysis on the PSR J1125–6014 timing residuals shows that the noise model with the white noise and the DM noise parameters had the highest Bayesian evidence. We derive and constrain the mass of the pulsar to be  $M_p = 1.68 \pm 0.17 M_\odot$ . The companion mass and the orbital inclination angle are constrained to be  $M_c = 0.33 \pm 0.02 M_\odot$  and  $i = 77.6 \pm 0.8^\circ$ , respectively. In Figure C1 of Appendix C, the posterior probability distributions of the measured Shapiro parameters are presented as well as the derived masses and inclination angles for PSR J1125–6014. We discuss the nature of this system in more detail in Section 5.

#### 4.1.4 PSR J1514–4946

PSR J1514–4946 is an MSP with a spin period of 3.59 ms in a 1.92 d orbit. It is an unknown source in the first *Fermi* Large Area Telescope catalog (Abdo et al. 2010), and was confirmed as an MSP with the Parkes radio telescope by Kerr et al. (2012). Its phase-connected timing solution was later determined by Camilo et al. (2015). We performed a noise analysis on the PSR J1514–4946 timing residuals and obtained the same Bayesian evidences for noise models with DM, red, and white noise parameters. Therefore, we chose the noise model contained only the white noise parameters as it is the simplest one. We obtained a log Bayes factor of  $\ln \mathcal{B} \sim 6$  by comparing the timing models with and without the Shapiro parameters, showing that we detected a weak Shapiro signature in the timing residuals. Using the  $\chi^2$  analysis aforementioned in 4.1, we place a constraint on  $\cos i$  to be in the range of  $0.14 \leq \cos i \leq 0.28$  if  $M_p = 1.2 M_\odot$ , and  $0.21 \leq \cos i \leq 0.36$  if  $M_p = 2.0 M_\odot$ . The corresponding companion mass for the pulsar mass of  $M_p = 1.2 M_\odot$  found to be in the ranges of  $0.15 M_\odot \leq M_c \leq 0.17 M_\odot$  and  $73^\circ \leq i \leq 82^\circ$ , and for the pulsar mass of  $M_p = 2.0 M_\odot$  found to be in the ranges of  $0.22 M_\odot \leq M_c \leq 0.24 M_\odot$  and  $68^\circ \leq i \leq 78^\circ$ , respectively. These values of  $M_c$  are consistent with the Tauris & Savonije (1999) prediction for a He WD companion.

#### 4.1.5 PSR J1614–2230

PSR J1614–2230 is an MSP with a spin period of 3.15 ms in a 8.69 d orbit. Crawford et al. (2006) discovered PSR J1614–2230 after conducting an intermediate-latitude Galactic survey of 56 unidentified  $\gamma$ -ray sources from the third Energetic Gamma-Ray Experiment Telescope catalog (Hartman et al. 1999) with the 13 beam Parkes multibeam receiver at 1400 MHz (Hessels et al. 2005; Crawford et al. 2006). The precise Shapiro delay measurement, and high mass derived for PSR J1614–2230 carried out by Demorest et al. (2010) was able to reject many of the EOSs of the nuclear matter. Among our pulsars, PSR J1614–2230 has the most significant Shapiro delay detection:  $h_3 = 2.340 \pm 0.019 \mu\text{s}$  and  $\zeta = 0.9858 \pm 0.0003$ . These led us to constrain the mass of the pulsar to be  $M_p = 1.94 \pm 0.03 M_\odot$ , the companion mass to be  $M_c = 0.495 \pm 0.005 M_\odot$ , and the orbital

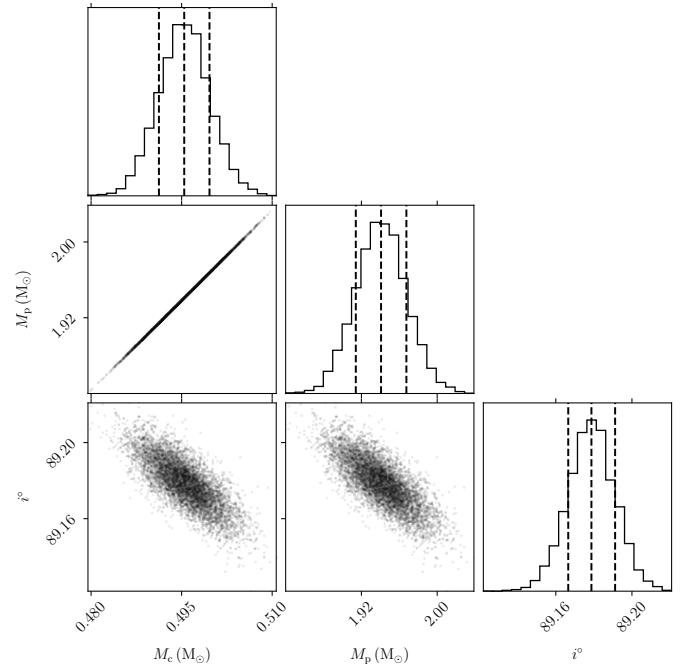


**Figure 1.** 2D marginalized posterior probability distributions of  $M_p$ ,  $M_c$ , and  $i$  (derived from measured  $h_3$  and  $\zeta$ ) for J1614–2230.

inclination angle to be  $i = 89.179^\circ \pm 0.013^\circ$ . Figure 1 shows the correlations between these parameters. The timing residuals, pre- and post-fitting, are shown in Figure 2. The posterior probability distributions of  $h_3$  and  $\zeta$ , as well as  $M_c$ ,  $M_p$ , and  $i$  that are derived from  $h_3$  and  $\zeta$ , are plotted in Figure C2 of Appendix C. For PSR J1614–2230, the noise model containing the DM noise, red noise, and white noise parameters had the highest Bayesian evidence.

#### 4.1.6 PSR J1732–5049

PSR J1732–5049 is an MSP with a spin period of 5.31 ms in a 5.26 d orbit. It is one of the nine pulsars discovered by Edwards & Bailes (2001) in an intermediate-latitude Galactic survey with a centre frequency near 1400 MHz conducted with the Parkes radio telescope. From our timing noise analysis, we obtained the highest evidence for the noise model containing the red noise and white noise parameters. Comparing the timing solutions with and without the Shapiro parameters, PSR J1732–5049 showed a likely Bayesian evidence for the presence of a Shapiro signature with a log Bayes factor of  $\log \mathcal{B} \sim 6$ . Using the  $\chi^2$  analysis mentioned in 4.1, we place a constraint on  $\cos i$  to be in the range of  $0.31 \leq \cos i \leq 0.47$  if  $M_p = 1.2 M_\odot$ , and  $0.35 \leq \cos i \leq 0.51$  if  $M_p = 2.0 M_\odot$ . The corresponding companion mass for the pulsar mass of  $M_p = 1.2 M_\odot$  was found to be in the ranges of  $0.17 M_\odot \leq M_c \leq 0.20 M_\odot$  and  $61^\circ \leq i \leq 72^\circ$ , and for the pulsar mass of  $M_p = 2.0 M_\odot$  found to be in the ranges of  $0.24 M_\odot \leq M_c \leq 0.27 M_\odot$  and  $59^\circ \leq i \leq 70^\circ$ , respectively. These values of  $M_c$  are consistent with the Tauris & Savonije (1999) prediction for a He WD companion.

#### 4.1.7 PSR J1909–3744

PSR J1909–3744 is an MSP with a spin period of 2.95 ms in a 1.53 d orbit. The Swinburne High Latitude Pulsar Survey was a blind survey

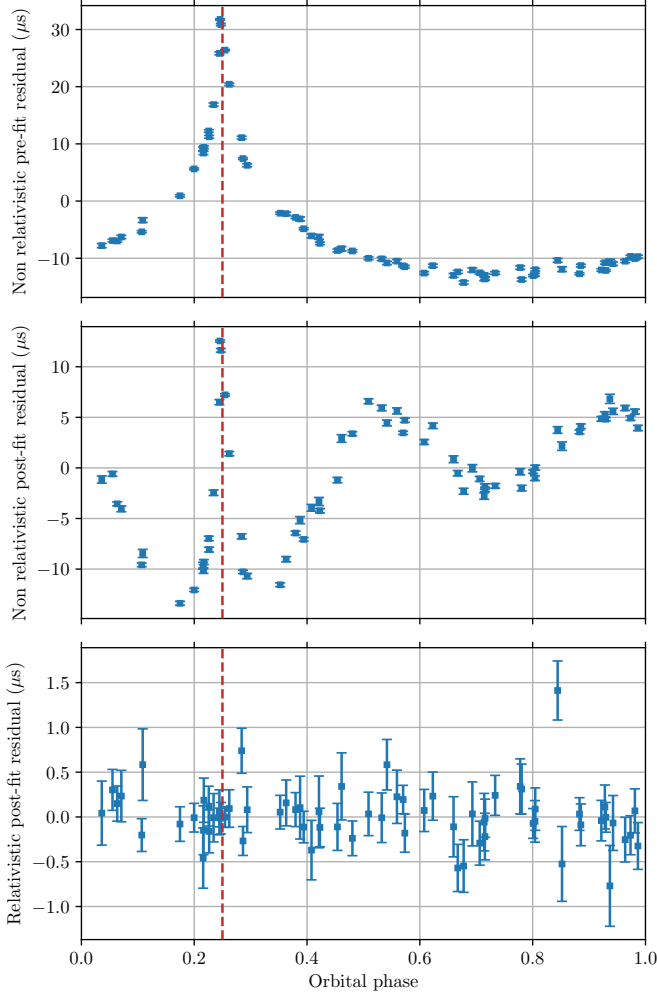


**Figure 2.** Pre- and post-fit timing residuals as a function of orbital phase for J1614–2230. The top panel shows the actual Shapiro delay signature preserved in the pre-fit timing residuals (excluding relativistic effects from the timing model). The middle panel shows the timing residuals after fitting for the non-relativistic orbital parameters. The bottom panel shows the timing residuals after fitting for all the parameters. The superior conjunction happens at the orbital phase of 0.25 and is indicated by the vertical dashed red line.

that led Jacoby et al. (2003) to discover PSR J1909–3744 using the Parkes 13-beam multibeam receiver. The noise model including DM noise, red noise, and white noise parameters had the highest evidence, and our constraints on the orthometric Shapiro parameters were  $h_3 = 0.845 \pm 0.007 \mu\text{s}$  and  $\varsigma = 0.9441 \pm 0.0016$ . We derive and constrain the mass of the pulsar to be  $M_p = 1.45 \pm 0.03 M_\odot$ . The companion mass and the orbital inclination angle are constrained to be  $M_c = 0.205 \pm 0.003 M_\odot$  and  $i = 86.69^\circ \pm 0.10$ , respectively. The posterior probability distribution of the measured and derived parameters can be found in the Figure C3 of Appendix C. The companion mass is consistent with the predictions of Tauris & Savonije (1999) for a He WD, and is the first confirmation of this mass relation.

## 4.2 The uncertainty in the pulsar mass as a function of $\cos(i)$

While it is unfortunate that not all pulsar binaries are in edge-on systems, it is not surprising. Here we explore the  $(M_c, \sin i)$  space

**Table 1.** Pulsar and companion star masses and inclination angles. The derived inclination angles have another equally likely solution of  $180^\circ - i$ . The pulsars with two entries could not have their pulsar masses well determined and so two possible (small and large) pulsar masses were held fixed and likely companion and inclination angles provided for them.

Pulsar	$M_p (M_\odot)$	$M_c (M_\odot)$	$\cos i$	$i^\circ$
J0101–6422	1.2	0.14–0.16	0.24–0.28	73–75
	2.0	0.20–0.22	0.29–0.34	70–74
J1101–6424	1.2	0.51–0.59	0.47–0.60	53–62
	2.0	0.74–0.87	0.55–0.67	47–57
J1125–6014	$1.68^{+0.17}_{-0.15}$	$0.33^{+0.02}_{-0.02}$	$0.215^{+0.013}_{-0.012}$	$77.6^{+0.7}_{-0.8}$
J1514–4946	1.2	0.15–0.17	0.14–0.28	73–82
	2.0	0.22–0.24	0.21–0.36	68–78
J1614–2230	$1.94^{+0.03}_{-0.03}$	$0.495^{+0.005}_{-0.005}$	$0.0143^{+0.0002}_{-0.0002}$	$89.179^{+0.013}_{-0.013}$
J1732–5049	1.2	0.17–0.20	0.31–0.47	61–72
	2.0	0.24–0.27	0.35–0.51	59–70
J1909–3744	$1.45^{+0.03}_{-0.03}$	$0.205^{+0.003}_{-0.003}$	$0.0573^{+0.0016}_{-0.0016}$	$86.69^{+0.10}_{-0.10}$

where meaningful Shapiro delays can be detected through simulation. For an arbitrary binary that we simulate, we wanted to understand what the companion mass error ( $\sigma_{M_c}$ ) and  $\sin i$  error ( $\sigma_{\sin i}$ ) are by holding the pulsar mass, companion mass, and orbital period fixed, and then use them to understand what the pulsar mass error ( $\sigma_{M_p}$ ) would be after the fit.

Using TEMPO2’s fake plugin, we conducted two sets of simulations. In both simulations, we have used ELL1 binary model. In the first, we investigated how  $\sigma_{M_c}$  and  $\sigma_{\sin i}$  generally change as a function of  $\cos i$ . Then we used equations 11 and 13 in order to predict  $\sigma_{M_p}$ . The results of this simulation provides a mathematical relation by which the error in the pulsar mass  $\sigma_{M_p}$  can be estimated.

### 4.2.1 Constant $M_c$ and $M_p$

In the first set of simulations, we aimed to perform the analysis of measuring  $\sigma_{M_p}$  as we are rotating the orbit in a way that the inclination angle of the orbit changes with respect to our line of sight. We took our timing solution for J1614–2230, removed the dispersion measure and the noise parameters, and used it to simulate ToAs. Using Equation 11, the projected semi-major axis of the pulsar at different inclination angles from  $45^\circ$  to  $89^\circ$ , given the pulsar mass of  $2.0 M_\odot$  and the companion mass of  $1.0 M_\odot$ , were calculated. Then 1300 ToAs with the root-mean-square (rms) residuals of  $0.1 \mu\text{s}$  were simulated (similar to what can be obtained for some MSPs in a reasonable time), and using TEMPNEST we sampled the binary parameters including  $P_b, T_{\text{asc}}, x, \epsilon_1, \epsilon_2, M_c$ , and  $\sin i$  and recorded the values and errors of  $\sin i, M_c$ , and  $\text{Cov}[M_c, \sin i]$ . For every inclination angle, the simulation was repeated 10 times. In panel (a) of Figure 3, the value and the error bar of every point is, respectively, the average and the  $1\sigma$  standard deviation of  $\sigma_{\sin i}$  taken from 10 TEMPNEST runs. The same procedure was used for  $\sigma_{M_c}$ ,  $\text{Cov}[M_c, \sin i]$ , and  $\sigma_{M_p}$  in the panels (a), (b), (c), respectively. For every TEMPNEST run,  $\sigma_{M_p}$  was calculated using Equation 13.

We next derived empirical relationships between  $\cos i$  and  $\sigma_{\sin i}$ ,  $\sigma_{M_c}$ , and  $\text{Cov}[M_c, \sin i]$ . We found that the best fitting function to the relationships was of the polynomial form

$$\mathcal{F}(\cos i) = \sum_{j=0}^n a_j \cos^j i, \quad (16)$$

where the coefficients of  $a_j$  for  $\sigma_{M_c}$  fitting function ( $\mathcal{F}_{\sigma_{M_c}}$ ),  $\sigma_{\sin i}$  fitting function ( $\mathcal{F}_{\sigma_{\sin i}}$ ), and  $\text{Cov}[M_c, \sin i]$  fitting function

**Table 2.** Fitting results for the error modelling.

coefficient	$\mathcal{F}_{\sigma_{\sin i}}$	$\mathcal{F}_{\sigma_{M_c}}$	$\mathcal{F}_{\text{Cov}[M_c, \sin i]}$
$a_0$	$-1.7(4) \times 10^{-6}$	0.00363(10)	$-9(11) \times 10^{-9}$
$a_1$	$4.3(6) \times 10^{-4}$	0.116(9)	$2(2) \times 10^{-6}$
$a_2$	0.014(2)	-0.7(2)	$-2.6(11) \times 10^{-4}$
$a_3$	0.10(3)	7.0(19)	3(3)
$a_4$	0.10(15)	-22(7)	-0.05(2)
$a_5$	0.4(2)	27(8)	0.17(9)
$a_6$	—	—	-0.38(13)

( $\mathcal{F}_{\text{Cov}[M_c, \sin i]}$ ) can be found by minimizing the sum of least squares. The number of coefficients depends on the orbital inclination angle. We found that, for  $0.01 \leq \cos i \leq 0.16$ , we need at least a third order polynomial ( $n = 3$ ). By increasing the range of  $\cos i$  to be in  $0.01 \leq \cos i \leq 0.35$ , corresponding to the orbital inclination angle of  $70^\circ \leq i < 90^\circ$ , we need to have at least six coefficients. We used the latter case in our modeling of uncertainties, and found the constant coefficients of  $a_0, \dots, a_5$  in Table 2 for  $\mathcal{F}_{\sigma_{\sin i}}$  (the dashed line in the panel (a) of Figure 3),  $\mathcal{F}_{\sigma_{M_c}}$  (the dashed line in the panel (b) of Figure 3), and  $\mathcal{F}_{\text{Cov}[M_c, \sin i]}$  (the dashed line in the panel (c) of Figure 3). We then used Equation 13 and substituted  $\sigma_{M_c}$ ,  $\sigma_{\sin i}$ , and  $\text{Cov}[M_c, \sin i]$  with  $\mathcal{F}_{\sigma_{M_c}}$ ,  $\mathcal{F}_{\sigma_{\sin i}}$ , and  $\mathcal{F}_{\text{Cov}[M_c, \sin i]}$ , respectively, to find the modeled error in the pulsar mass (the dashed line in the panel (d) of Figure 3). We also explored how  $\sigma_{\sin i}$ ,  $\sigma_{M_c}$ , and  $\text{Cov}[M_c, \sin i]$  scale with the rms residuals of 1 and  $2 \mu\text{s}$ , the companion masses of 0.2 and  $0.5 M_\odot$ , and with 2600 ToAs (2 times the initial number of ToAs). The results show that  $\sigma_{\sin i}$ ,  $\sigma_{M_c}$ , and  $\text{Cov}[M_c, \sin i]$  are scaled with the following relations:

$$\sigma_{\sin i} = \left( \frac{M_\odot}{M_c} \right) \left( \frac{\sigma_{\text{rms}}}{\mu\text{s}} \right) \left( \frac{1000}{N_{\text{ToA}}} \right)^{\frac{1}{2}} \mathcal{F}_{\sigma_{\sin i}}(\cos i), \quad (17)$$

$$\sigma_{M_c} = \left( \frac{\sigma_{\text{rms}}}{\mu\text{s}} \right) \left( \frac{1000}{N_{\text{ToA}}} \right)^{\frac{1}{2}} \mathcal{F}_{\sigma_{M_c}}(\cos i), \quad (18)$$

and

$$\text{Cov}[M_c, \sin i] = \left( \frac{M_\odot}{M_c} \right) \left( \frac{\sigma_{\text{rms}}}{\mu\text{s}} \right)^2 \left( \frac{1000}{N_{\text{ToA}}} \right) \mathcal{F}_{\text{Cov}[M_c, \sin i]}(\cos i). \quad (19)$$

We used our model to calculate  $\sigma_{M_p}$  for both PSRs J1614–2230 and J1909–3744. Because the ToA uncertainties range from 201 ns to  $7.6 \mu\text{s}$  for PSR J1614–2230, and from 9 ns to  $2.2 \mu\text{s}$  for PSR J1909–3744, we needed to create ToAs that are averaged in time. We averaged to 4 min (the observing length of typical observations), and then calculated the number of unique averaged ToAs and the weighted rms of the residuals. After averaging, for PSR J1614–2230 we obtained a weighted rms residual of  $0.310 \mu\text{s}$  for 119 observations, and for PSR J1909–3744 we obtained a weighted rms residual of  $0.125 \mu\text{s}$  for 179 observations. Using our model, we determined  $\sigma_{M_p}$  to be  $\sim 0.03 M_\odot$  for both, which is in very good agreement with the measured  $\sigma_{M_p}$  of  $0.03 M_\odot$  in Table 1.

We are able to use our model to estimate  $\sigma_{M_p}$  in PSR J0101–6422 and J1514–4946, but not in PSRs J1101–6424 and J1732–5049, because our model is only reliable for  $\cos i < 0.35$ . For PSR J0101–6422 and J1514–4946, if we assume  $M_p = 1.4 M_\odot$ , by taking the median values of  $\cos i$  to be 0.27 and 0.22, resulting in the companion masses to be  $0.17 M_\odot$  and  $0.18 M_\odot$ , we estimated  $\sigma_{M_p}$  to be  $1.6 M_\odot$  and  $0.8 M_\odot$ , respectively. If we assume  $M_p = 2.0 M_\odot$ ,

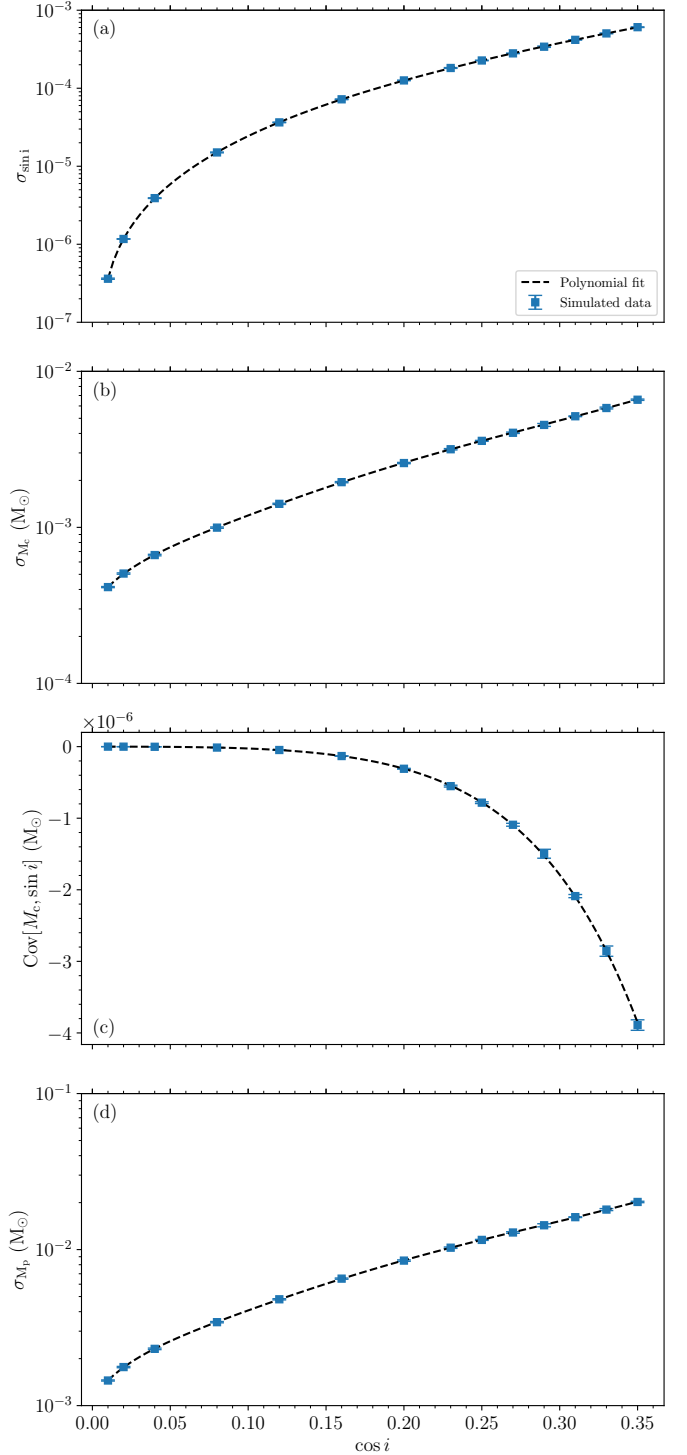


**Figure 3.** Exploring the error in the component masses at different orbital inclination angles using 1300 simulated ToAs with the rms residuals of  $0.1 \mu\text{s}$ , for a binary pulsar system with the companion mass of  $1 M_\odot$ , the pulsar mass of  $2.0 M_\odot$ , and the orbital period of 8.69 d. (a): the error in the sine of the orbital inclination angle. (b): the error in the companion mass. (c): the covariance between the companion mass and the sine of the orbital inclination angle. (d): the error in the pulsar mass. The dashed lines in panels (a), (b), and (c) are the polynomial functions described by Equations 17, 18, 19, respectively, and the coefficients for each are listed in Table 2. The dashed line in the bottom panel is calculated using Equation 13.



by taking the median values of  $\cos i$  to be 0.30 and 0.27, resulting in the companion masses to be  $0.21 M_\odot$  and  $0.23 M_\odot$ , we estimated  $\sigma_{M_p}$  to be  $2.0 M_\odot$  and  $1.3 M_\odot$ , respectively.

#### 4.2.2 Constant $f_m$

Soon after a binary pulsar is discovered, the mass function is quickly (and accurately) established, and so we also wanted to explore what the likely  $\sigma_{M_p}$  would be if the pulsar mass and mass function are held fixed and we have no a priori knowledge of the inclination angle. This simulation method can be used whenever a new millisecond pulsar is discovered, the mass function is known, and observers want to determine the chance of being able to measure a significant Shapiro delay for various inclination angles (and hence component masses). In this second set of simulations, we thus investigated how  $\sigma_{M_p}$  depended upon the known mass functions in PSRs J0101–6422, J1101–6424, J1514–4946, and J1732–5049 if  $80^\circ \leq i < 90^\circ$ , corresponding to  $\sim 0.0 \leq \cos i \leq 0.16$ . We did not explore higher  $\cos i$  values as beyond this  $\sigma_{M_p}$  becomes larger than  $2.0 M_\odot$ . The companion mass values were calculated at different inclination angles using Equation 11, assuming the mass function of each pulsar and  $M_p = 1.5 M_\odot$ . We then simulated 1300 ToAs with the rms residuals of data in the Tables A1 and A2. The same procedure as Section 4.2.1 was used for performing the timing analysis, and plotting the errors. The only difference was, at every inclination angle, the simulation was repeated 100 times.

In Figure 4, PSR J1101–6424 has the largest uncertainties in  $\sin i$  and  $M_c$  due to its high rms residuals of  $7.973 \mu\text{s}$  despite its massive companion. In our timing analysis for PSRs J0101–6422, J1101–6424, J1514–4946, and J1732–5049, we were interested in getting  $\sigma_{M_p} \leq 0.1 M_\odot$  to be astrophysically interesting. However, from Figure 4, the orbital inclination angles of PSRs J0101–6422 and J1514–4946 systems need to have  $\cos i \leq 0.01$  to achieve this, given our timing precision. PSRs J1101–6424 and J1732–5049 have  $\sigma_{M_p}$  greater than  $0.1 M_\odot$  at all values of  $\cos i$ . From the  $\chi^2$  analysis in 4.1, all four pulsars have  $\cos i$  greater than 0.16, which stops us from placing meaningful constraints on their pulsar masses.

## 5 DISCUSSION

### 5.1 Comparison with previous measurements

We now check whether our results are consistent with those obtained by other authors, in a historical sequence.

#### 5.1.1 PSR J1909–3744

From the NANOGrav 11 yr data release, Arzoumanian et al. (2018) measured the Shapiro delay using the traditional parameterisation ( $M_c, \sin i$ ) for PSR J1909–3744 and estimated the parameters of  $M_p = 1.48 \pm 0.03 M_\odot$ ,  $M_c = 0.208 \pm 0.002 M_\odot$ , and  $i = 86.47^\circ \pm 0.10^\circ$ . Liu et al. (2020) used 15 yr of PSR J1909–3744 observations with Nancay Radio Telescope to perform a high-precision analysis, and derived a pulsar mass of  $M_p = 1.492 \pm 0.014 M_\odot$  and a companion mass of  $M_c = 0.209 \pm 0.001 M_\odot$  using the traditional parameterisation. Another independent analysis of J1909–3744 used 15 yr of PPTA-DR2e (Reardon et al. 2021) to measure the Shapiro delay parameters and obtained  $M_p = 1.486 \pm 0.011 M_\odot$ ,  $M_c = 0.2081 \pm 0.0009 M_\odot$ ,  $i = 86.46^\circ \pm 0.05^\circ$ . Using the International Pulsar Timing Array second data release (consisting of data sets collected by PPTA, the European pulsar timing array, and NANOGrav)

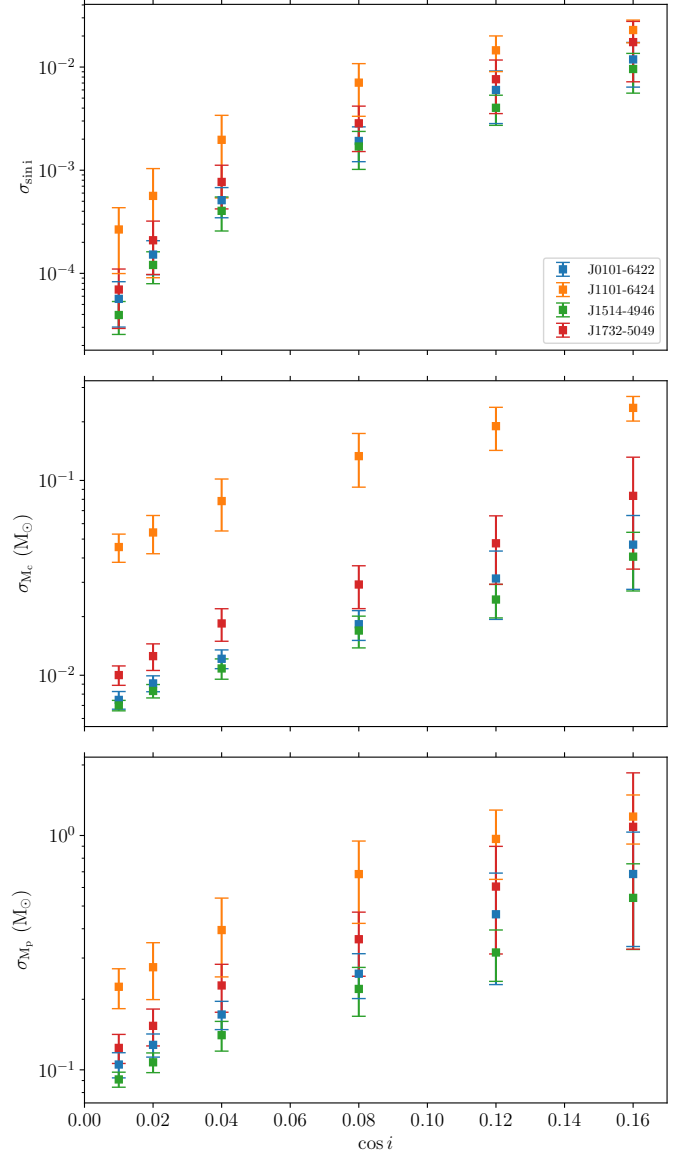


**Figure 4.** Error in the component masses at different orbital inclination angles for PSRs J0101–6422, J1101–6424, J1514–4946, and J1732–5049 using 1300 simulated ToAs with the rms of the actual data. Top: the error in the sine of orbital inclination angle. Middle: the error in the companion mass. Bottom: the error in the pulsar mass. The colors indicate the different binary pulsar systems of PSRs J0101–6422 (blue), J1101–6424 (orange), J1514–4946 (green), and J1732–5049 (red). The mass of the pulsar is assumed to be  $1.5 M_\odot$  in all the simulations.

Perera et al. (2019) analyzed 10.8 yr of data and provided measurements of the classical Shapiro parameters of  $M_c = 0.209 \pm 0.001 M_\odot$  and  $\sin i = 0.99807 \pm 0.00006$  for PSR J1909–3744. Using the mass function from `psrcat`<sup>7</sup> and applying Equations 11 and 13, we can derive the pulsar mass to be  $M_p = 1.496 \pm 0.011 M_\odot$ . Our derived masses and the inclination angle for PSR J1909–3744 (from the Table 1) are:  $M_p = 1.45 \pm 0.03 M_\odot$ ,  $M_c = 0.205 \pm 0.003 M_\odot$ ,  $i = 86.69^\circ \pm 0.10^\circ$ . Our masses are approximately  $1\sigma$  smaller than previously reported values.

<sup>7</sup> <https://www.atnf.csiro.au/research/pulsar/psrcat>

### 5.1.2 PSR J1614–2230

The analysis of the PSR J1614–2230 system by [Demorest et al. \(2010\)](#) utilized a set of observations from the Green Bank Telescope to constrain the Shapiro delay using the classic parameterisation:  $M_p = 1.97 \pm 0.04 M_\odot$ ,  $M_c = 0.500 \pm 0.006 M_\odot$ ,  $i = 89.17^\circ \pm 0.02^\circ$ . In a subsequent analysis, [Fonseca et al. \(2016\)](#) used the NANOGrav 9 yr data set, including a part of the data set used by [Demorest et al. \(2010\)](#), and made significant measurements of the Shapiro delay using both the classic and the orthometric parameterisations:  $M_p = 1.928 \pm 0.017 M_\odot$ ,  $M_c = 0.493 \pm 0.003 M_\odot$ ,  $i = 89.189^\circ \pm 0.014^\circ$ . Then [Arzoumanian et al. \(2018\)](#) used the NANOGrav 11 yr data set and put constraints on the Shapiro delay using the orthometric parameterisation obtaining:  $M_p = 1.908 \pm 0.016 M_\odot$ ,  $M_c = 0.493 \pm 0.003 M_\odot$ ,  $i = 89.204^\circ \pm 0.014^\circ$ .

Our reported masses and the inclination angle for PSR J1614–2230 (from the Table 1) are:  $M_p = 1.94 \pm 0.03 M_\odot$ ,  $M_c = 0.495 \pm 0.005 M_\odot$ ,  $i = 89.179^\circ \pm 0.013^\circ$ . These are the first independent measurement using MTPA data sets and are in good agreement with the previous measurements reported.

The discovery of PSR J1614–2230 is important for reasons beyond the implications for the study of the EOS of dense matter: it was also important to establish that neutron stars can be born with large masses. [Tauris et al. \(2011\)](#) carried out a detailed study on modeling the formation and evolution of PSR J1614–2230 based on its physical parameters reported by [Demorest et al. \(2010\)](#). They investigated the evolution of PSR J1614–2230 using an evolving intermediate-mass X-ray binary and reported two possible scenarios: 1) through a common envelope started with their “Case C” RLO 2) through the highly super-Eddington isotropic re-emission mode during their “Case A” RLO, with the conclusion of the second scenario as the more likely one and the mass of the PSR J1614–2230 progenitor to be higher than  $20 M_\odot$ , and the initial companion to be a main-sequence donor star with the mass of  $4.0 - 5.0 M_\odot$ .

Because in Case A RLO the mass transfer happens while the companion is in the main sequence, the recycling episode is very long; providing a better explanation for the spin period of PSR J1614–2230, which is unusually small compared to all other pulsars with massive WDs. Interestingly, they find that even with the long accretion episode of Case A RLO, the total mass transfer is very small, less than  $0.3 M_\odot$ . This means that the birth mass was at least  $\sim 1.7 M_\odot$ . This is a strong indication that neutron star masses are generally acquired at birth, and don’t owe much to subsequent evolution.

Our measurements confirm their interpretation of the mass of PSR J1614–2230 system. The idea that neutron stars have high masses at birth was later confirmed with greater confidence by the discovery of massive neutron stars where little or no accretion happened, like PSR J2222–0137 ([Cognard et al. 2017](#); [Guo et al. 2021](#)), and further by measurement of the mass of PSR J1933–6211, which is thought to have evolved from case A RLO and nevertheless has a low mass, confirming that not much mass was transferred during its long evolutionary episode (Geyer et al., submitted).

### 5.1.3 PSR J1125–6014

From the the second data release of the Parkes Pulsar Timing Array (PPTA-DR2e), [Reardon et al. \(2021\)](#) performed an analysis of the PSR J1125–6014 system using more than 12 yr of data (a factor of four larger than the time span of PSR J1125–6014 observations with MeerKAT), and they constrained the pulsar mass, the companion mass, and the orbital inclination angle to be  $M_p = 1.5 \pm 0.2 M_\odot$ ,

$M_c = 0.31 \pm 0.03 M_\odot$ ,  $i = 77.9^{+1.4}_{-1.3}$ , respectively. Our derived masses and the inclination angle for PSR J1125–6014 (from the Table 1) are  $M_p = 1.68^{+0.17}_{-0.15} M_\odot$ ,  $M_c = 0.33 \pm 0.02 M_\odot$ ,  $i = 77.6^{+0.7}_{-0.8}$ , which are in good agreement with [Reardon et al. \(2021\)](#).

The mass of the companion of PSR J1125–6014 is significantly higher than the prediction of [Tauris & Savonije \(1999\)](#) for the orbital period of this system ( $0.25 M_\odot$ ). This suggests that the companion is not likely a Helium WD, but instead a low-mass CO WD. Interestingly, the short spin period of this pulsar and the high degree of recycling also suggest a case A RLO evolution, making the system a less massive version of PSR J1614–2230. We note in this regard the similarity of the orbital periods (both  $\sim 8.7$  d) and orbital eccentricities of the two systems.

## 5.2 Mass measurements with Shapiro delay

As an application of our error model, we can assess the fraction of MSPs for which we expect the masses to be measured to better than 10% using the Shapiro delay method. For a sample of 100 randomly oriented MSPs, each with a pulsar mass of  $1.4 M_\odot$ , 1300 ToAs, and the rms residuals of  $1 \mu s$ , we would expect to measure approximately 11 MSP masses to better than 10%, assuming the companion masses are all  $0.2 M_\odot$ . If we increase the companion mass to be  $0.4 M_\odot$ , we expect to measure up to 19 MSP masses to this accuracy. Regarding this, the maximum angles that we expect the systems to be inclined at are  $\sim 84^\circ$  and  $79^\circ$  for the MSP systems with companion masses of  $0.2 M_\odot$  and  $0.4 M_\odot$ , respectively. Therefore, the fraction of the MSPs in a MSP sample for which we expect to measure their masses to this accuracy using the Shapiro delay method is low.

## 5.3 The mass distribution for WD companions to pulsars

For all known pulsars that are located outside of globular clusters and whose companions are found to be WDs, we have plotted the precisely measured masses (with the pulsar mass uncertainty less than 15%), with logarithmic scaled coloured circles indicating the pulsar spin period, in the panel (a) of Figure 5, as an update on Figure 6 in [McKee et al. \(2020\)](#).

In that reference, they indicated two main populations in their plot: 1) systems with companions less massive than  $0.46 M_\odot$  as low-mass helium WD stars 2) systems with companion masses between  $0.7 - 0.9 M_\odot$  as carbon oxygen WD stars. One of the conclusions is that there is a mass gap between  $0.41$  and  $0.7 M_\odot$ . In addition to these, there are five special systems with less common types of evolution.

First, in the case of PSR J1141–6545 and B2303+46, the WDs formed before the pulsar; this is the reason why these systems have eccentric orbits as their pulsars have not been recycled ([van Kerkwijk & Kulkarni 1999](#); [Tauris & Sennels 2000](#)), and are therefore significantly slower (see panel (b) of Figure 5). The remaining three systems have low-eccentricity systems and recycled pulsars. As discussed previously, PSR J1614–2230 is a rare system with a heavy neutron star and a carbon-oxygen WD, thought to have been formed in Case A RLO ([Tauris et al. 2011](#)). PSR J0348+0432 is a massive pulsar with a low-mass WD companion, has a tight orbit of 2.4 hr, and the WD probably did not have an envelope mass less than the critical limit for hydrogen fusion, based on the assumption of [Antoniadis et al. \(2013\)](#). This pulsar is unusually slow for such a tight orbit and such a low-mass companion. Finally, PSR J2222–0137 has a very massive ( $M_{WD} = 1.3194 \pm 0.0040 M_\odot$ , [Guo et al. 2021](#)) and cool ([Kaplan et al. 2014](#)) WD companion.

We have explored where PSRs J1125–6014, J1614–2230, and

J1909–3744 lie in Fig 5 relative to the other pulsars. They are very consistent with the established distribution of the pulsars and WDs as discussed in McKee et al. (2020). PSR J1125–6014 is starting to fill an empty region of parameter space close to PSR J1614–2230, possibly because it also formed via Case A RLO.

Figure 5 highlights the apparent gap between the masses of the MSPs with 0.15–0.5  $M_{\odot}$  (this is even wider if we exclude binaries formed in Case A RLO), and those between 0.7 and 0.9  $M_{\odot}$ . Are there WD companions to neutron stars with masses in between? If not, this would suggest that we have a higher probability of measuring a Shapiro delay when the mass function yields  $0.7 < M_c < 0.9 M_{\odot}$ , assuming  $i = 90^{\circ}$ . However, it is important to attempt to measure the Shapiro delay in systems where the mass function suggests intermediate masses in order to test the idea that there is indeed a gap in WD masses between 0.4 and 0.7  $M_{\odot}$ .

In panel (b) of Figure 5, we have also plotted the precisely measured companion mass versus pulsar spin period. For the bulk of the recycled pulsars there is a strong correlation between the companion mass and the log of the spin period. This is expected from basic considerations of stellar evolution: the more massive WD companions had more massive progenitors, which have evolved faster. Because of this faster evolution, the time available for mass transfer and accretion is much smaller; resulting in smaller ablation of the B-field and a smaller amount of spin-up. The exceptions are PSR J0348+0242 and, as discussed before, PSR J1614–2230.

Sometimes extending the timing baseline with archival data can lead to increased accuracy of parameters that are undergoing secular changes, like position (via proper motion) and the time derivative of the projected semi-major axis. These can help limit the inclination angle from equation 12. We added 817 ToAs from 8.34 years of PPTA DR2e data sets of PSR J1732–5049 (Reardon et al. 2021) with an rms residuals of 4.471  $\mu$ s, to the current 4486 MeerKAT ToAs with an rms residuals of 2.3  $\mu$ s in order to try and constrain  $\dot{x}$  and find an upper limit on inclination angle; however, by using 18.97 years of data we could only gain an upper limit on the measured  $\dot{x} = 4(7) \times 10^{-16}$ , so we were still not be able to achieve this.

## 6 CONCLUSIONS

We have presented the timing analysis of seven MSPs using  $\sim 3$  years of MeerKAT observations, and provided updated timing models. We detected evidence for the relativistic Shapiro delay in the timing residuals of all MSPs. By conducting a Bayesian analysis, we were able to measure the Shapiro delay using the orthometric amplitude  $h_3$  and orthometric ratio  $\zeta$ . For PSRs J1125–6014, J1614–2230 and J1909–3744, we could constrain the mass of the pulsars to be  $M_p = 1.68^{+0.17}_{-0.15} M_{\odot}$ ,  $M_p = 1.94 \pm 0.03 M_{\odot}$  and  $M_p = 1.45 \pm 0.03 M_{\odot}$ , and the companion masses to be  $M_c = 0.33 \pm 0.02 M_{\odot}$ ,  $M_c = 0.495 \pm 0.005 M_{\odot}$  and  $M_c = 0.205 \pm 0.003 M_{\odot}$ , respectively. For pulsars with no meaningful mass constraints, 68% likelihood of the companion masses and the orbital inclination angles were calculated using  $\chi^2$  analysis, assuming fixed pulsar masses of 1.2  $M_{\odot}$  and 2.0  $M_{\odot}$ . We find that our mass measurements are in agreement with previous mass measurements for the same systems, and with the previously observed distribution of pulsar and WD masses.

We performed two series of simulations for exploring the change of errors in the Shapiro parameters,  $\sigma_{\sin i}$  and  $\sigma_{M_c}$ , at different orbital inclination angles, and derived the estimated errors in the pulsar mass  $\sigma_{M_p}$ . We then modeled the change of  $\sigma_{M_p}$  as a function of the cosine of the orbital inclination angle. This model works well for  $\cos i < 0.35$ . In addition, using our simulations, we demonstrated that, at

the likely inclination angles of the four systems, it was no surprise that their pulsar masses could not be determined. We provided an empirical polynomial formula that observers can use to estimate their likelihood of determining pulsar masses given good orbital coverage and the number and rms of timing residuals as a function of the orbital inclination angle.

## ACKNOWLEDGEMENTS

The MeerKAT telescope is operated by the South African Radio Astronomy Observatory, which is a facility of the National Research Foundation, an agency of the Department of Science and Innovation. MS, MB, DR, and RMS acknowledge support through the Australian Research Council Centre of Excellence for Gravitational Wave Discovery (OzGrav), through project number CE17010004. RMS acknowledges support through Australian Research Council Future Fellowship FT190100155. MK acknowledges significant support from the Max-Planck Society (MPG) and the MPIfR contribution to the PTUSE hardware. MCB, DJC, PCCF, AP and VVK acknowledges continuing support from MPG. AP acknowledges the using resources from the research grant “iPeska” (P.I. Andrea Possenti) funded under the INAF national call Prin-SKA/CTA approved with the Presidential Decree 70/2016. AP also had the support from the Ministero degli Affari Esteri e della Cooperazione Internazionale - Direzione Generale per la Promozione del Sistema Paese - Progetto di Grande Rilevanza ZA18GR02. This work used the OzSTAR national facility at Swinburne University of Technology. OzSTAR is funded by Swinburne University of Technology and the National Collaborative Research Infrastructure Strategy (NCRIS). This research has made use of NASA’s Astrophysics Data System and software such as: PSRCHIVE (van Straten et al. 2012), TEMPO2 (Hobbs et al. 2006; Edwards et al. 2006), TEMPO2 (Lentati et al. 2014), PULSEPORTRAITURE (Pennucci et al. 2014; Pennucci 2019), NUMPY (van der Walt et al. 2011), SCIPY (Virtanen et al. 2019), MATPLOTLIB (Hunter 2007), IPYTHON (Pérez & Granger 2007), ASTROPY (Astropy Collaboration et al. 2013, 2018), SCIKIT-LEARN (Pedregosa et al. 2011), corner.py (Foreman-Mackey 2016), and CMASHER (van der Velden 2020).

## DATA AVAILABILITY

Data is available from the Swinburne pulsar portal: <https://pulsars.org.au>

## REFERENCES

- Abdo A. A., et al., 2010, *ApJS*, **188**, 405
- Alpar M. A., Cheng A. F., Ruderman M. A., Shaham J., 1982, *Nature*, **300**, 728
- Antoniadis J., van Kerkwijk M. H., Koester D., Freire P. C. C., Wex N., Tauris T. M., Kramer M., Bassa C. G., 2012, *MNRAS*, **423**, 3316
- Antoniadis J., et al., 2013, *Science*, **340**, 448
- Antoniadis J., Tauris T. M., Ozel F., Barr E., Champion D. J., Freire P. C. C., 2016, arXiv e-prints, p. [arXiv:1605.01665](https://arxiv.org/abs/1605.01665)
- Antoniadis J., et al., 2022, *MNRAS*, **510**, 4873
- Arzoumanian Z., et al., 2018, *ApJS*, **235**, 37
- Arzoumanian Z., et al., 2020, *ApJ*, **905**, L34
- Astropy Collaboration et al., 2013, *A&A*, **558**, A33
- Astropy Collaboration et al., 2018, *AJ*, **156**, 123
- Bailes M., et al., 2020, *Publ. Astron. Soc. Australia*, **37**, e028

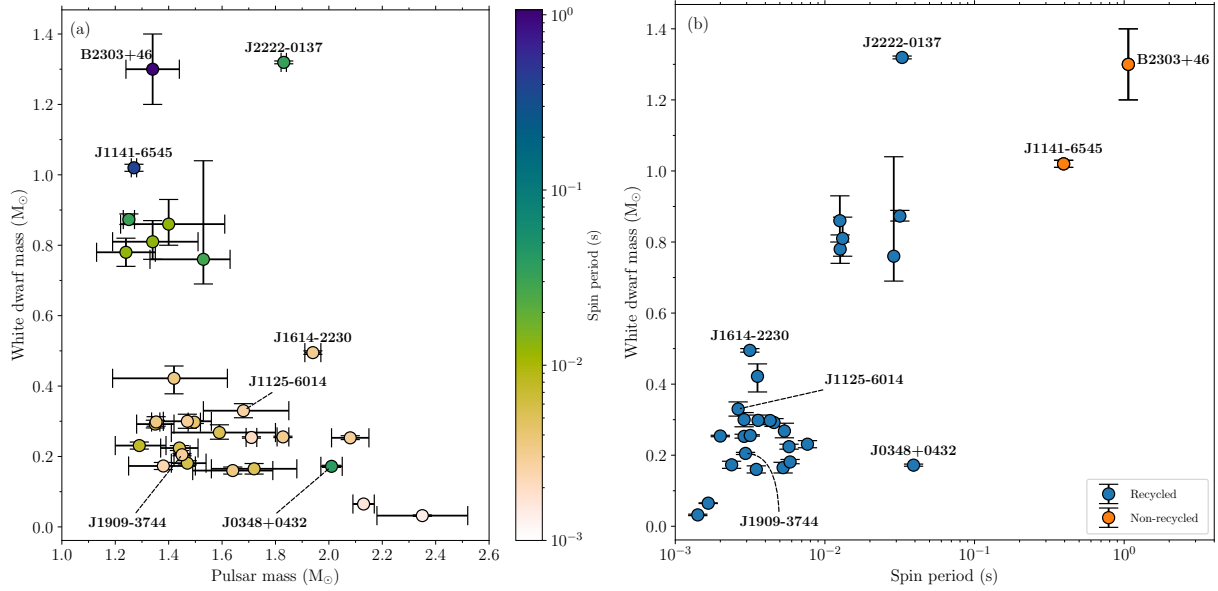


**Figure 5.** Precise mass measurements for all known pulsar-WD systems located outside of globular clusters. (a): Pulsar masses vs. white dwarf (WD) companion masses with coloured circles indicating the spin period of pulsars. (b): WD companion masses versus spin periods of pulsars. The values of the pulsar and WD masses as well as their references are listed in Table B1, and the spin periods are taken from psrcat.

Barr E. D., Freire P. C. C., Kramer M., Champion D. J., Berezina M., Bassa C. G., Lyne A. G., Stappers B. W., 2017, *MNRAS*, **465**, 1711  
 Berezina M., et al., 2017, *MNRAS*, **470**, 4421  
 Bhat N. D. R., Bailes M., Verbiest J. P. W., 2008, *Phys. Rev. D*, **77**, 124017  
 Camilo F., et al., 2015, *ApJ*, **810**, 85  
 Chalumeau A., et al., 2022, *MNRAS*, **509**, 5538  
 Cognard I., et al., 2017, *ApJ*, **844**, 128  
 Crawford F., Roberts M. S. E., Hessels J. W. T., Ransom S. M., Livingstone M., Tam C. R., Kaspi V. M., 2006, *ApJ*, **652**, 1499  
 Damour T., Deruelle N., 1986, *Ann. Inst. Henri Poincaré Phys. Théor.*, **44**, 263  
 Demorest P. B., Pennucci T., Ransom S. M., Roberts M. S. E., Hessels J. W. T., 2010, *Nature*, **467**, 1081  
 Demorest P. B., et al., 2013, *ApJ*, **762**, 94  
 Desvignes G., et al., 2016, *MNRAS*, **458**, 3341  
 Edwards R. T., Bailes M., 2001, *ApJ*, **553**, 801  
 Edwards R. T., Hobbs G. B., Manchester R. N., 2006, *MNRAS*, **372**, 1549  
 Faulkner A. J., et al., 2004, *MNRAS*, **355**, 147  
 Ferdman R. D., et al., 2010, *ApJ*, **711**, 764  
 Feroz F., Hobson M. P., 2008, *MNRAS*, **384**, 449  
 Feroz F., Hobson M. P., Bridges M., 2009, *MNRAS*, **398**, 1601  
 Fonseca E., Stairs I. H., Thorsett S. E., 2014, *ApJ*, **787**, 82  
 Fonseca E., et al., 2016, *ApJ*, **832**, 167  
 Fonseca E., et al., 2021, *ApJ*, **915**, L12  
 Foreman-Mackey D., 2016, *The Journal of Open Source Software*, **1**, 24  
 Freire P. C. C., 2022, arXiv e-prints, p. arXiv:2204.13468  
 Freire P. C. C., Wex N., 2010, *MNRAS*, **409**, 199  
 Goncharov B., et al., 2021, *ApJ*, **917**, L19  
 Guo Y. J., et al., 2021, *A&A*, **654**, A16  
 Hartman R. C., et al., 1999, *ApJS*, **123**, 79  
 Hessels J., Ransom S., Roberts M., Kaspi V., Livingstone M., Tam C., Crawford F., 2005, in Rasio F. A., Stairs I. H., eds, *Astronomical Society of the Pacific Conference Series Vol. 328, Binary Radio Pulsars*. p. 395 (arXiv:astro-ph/0404167)  
 Hobbs G., Dai S., 2017, arXiv e-prints, p. arXiv:1707.01615  
 Hobbs G. B., Edwards R. T., Manchester R. N., 2006, *MNRAS*, **369**, 655  
 Hu H., Kramer M., Wex N., Champion D. J., Kehl M. S., 2020, *MNRAS*, **497**, 3118  
 Hunter J. D., 2007, *Computing in Science & Engineering*, **9**, 90

Jacoby B. A., Bailes M., van Kerkwijk M. H., Ord S., Hotan A., Kulkarni S. R., Anderson S. B., 2003, *ApJ*, **599**, L99  
 Jacoby B. A., Hotan A., Bailes M., Ord S., Kulkarni S. R., 2005, *ApJ*, **629**, L113  
 Jones M. L., et al., 2017, *ApJ*, **841**, 125  
 Kandel D., Romani R. W., Filippenko A. V., Brink T. G., Zheng W., 2020, *ApJ*, **903**, 39  
 Kaplan D. L., et al., 2014, *ApJ*, **789**, 119  
 Kasian L. E., 2012, PhD thesis, University of British Columbia, Canada  
 Kass R. E., Raftery A. E., 1995, *Journal of the American Statistical Association*, **90**, 773  
 Keith M. J., et al., 2013, *MNRAS*, **429**, 2161  
 Kerr M., et al., 2012, *ApJ*, **748**, L2  
 Kiziltan B., Kottas A., De Yoreo M., Thorsett S. E., 2013, *ApJ*, **778**, 66  
 Kopeikin S. M., 1996, *ApJ*, **467**, L93  
 Kramer M., 2014, *International Journal of Modern Physics D*, **23**, 1430004  
 Kramer M., et al., 2006, *Science*, **314**, 97  
 Kramer M., et al., 2021a, *Physical Review X*, **11**, 041050  
 Kramer M., et al., 2021b, *MNRAS*, **504**, 2094  
 Krishnan V. V., 2019, PhD thesis, Swinburne University of Technology, Australia  
 Lange C., Camilo F., Wex N., Kramer M., Backer D. C., Lyne A. G., Doroshenko O., 2001, *MNRAS*, **326**, 274  
 Lattimer J. M., Prakash M., 2004, *Science*, **304**, 536  
 Lazarus P., Karuppusamy R., Graikou E., Caballero R. N., Champion D. J., Lee K. J., Verbiest J. P. W., Kramer M., 2016, *MNRAS*, **458**, 868  
 Lentati L., Alexander P., Hobson M. P., Feroz F., van Haasteren R., Lee K. J., Shannon R. M., 2014, *MNRAS*, **437**, 3004  
 Lentati L., et al., 2015, *MNRAS*, **453**, 2576  
 Liu K., et al., 2020, *MNRAS*, **499**, 2276  
 Lorimer D. R., 2008, *Living Reviews in Relativity*, **11**, 8  
 Mata Sánchez D., Istrate A. G., van Kerkwijk M. H., Breton R. P., Kaplan D. L., 2020, *MNRAS*, **494**, 4031  
 McKee J. W., et al., 2020, *MNRAS*, **499**, 4082  
 Miles M. T., Shannon R. M., Bailes M., Reardon D. J., Buchner S., Middleton H., Spiwak R., 2022, *MNRAS*, **510**, 5908  
 Ng C., et al., 2015, *MNRAS*, **450**, 2922  
 Özel F., Freire P., 2016, *ARA&A*, **54**, 401  
 Park R. S., Folkner W. M., Williams J. G., Boggs D. H., 2021, *AJ*, **161**, 105



- Pedregosa F., et al., 2011, *Journal of Machine Learning Research*, 12, 2825
- Pennucci T. T., 2019, *ApJ*, 871, 34
- Pennucci T. T., Demorest P. B., Ransom S. M., 2014, *ApJ*, 790, 93
- Perera B. B. P., et al., 2019, *MNRAS*, 490, 4666
- Pérez F., Granger B. E., 2007, *Computing in Science and Engineering*, 9, 21
- Radhakrishnan V., Srinivasan G., 1982, *Current Science*, 51, 1096
- Reardon D. J., et al., 2016, *MNRAS*, 455, 1751
- Reardon D. J., et al., 2021, *MNRAS*, 507, 2137
- Romani R. W., Kandel D., Filippenko A. V., Brink T. G., Zheng W., 2021, *ApJ*, 908, L46
- Romani R. W., Kandel D., Filippenko A. V., Brink T. G., Zheng W., 2022, *ApJ*, 934, L17
- Serylak M., et al., 2022, arXiv e-prints, p. [arXiv:2203.00607](https://arxiv.org/abs/2203.00607)
- Shannon R. M., et al., 2013, *Science*, 342, 334
- Shannon R. M., et al., 2015, *Science*, 349, 1522
- Shapiro I. I., 1964, *Phys. Rev. Lett.*, 13, 789
- Spiewak R., et al., 2022, arXiv e-prints, p. [arXiv:2204.04115](https://arxiv.org/abs/2204.04115)
- Splaver E. M., Nice D. J., Arzoumanian Z., Camilo F., Lyne A. G., Stairs I. H., 2002, *ApJ*, 581, 509
- Stairs I. H., 2003, *Living Reviews in Relativity*, 6, 5
- Stairs I. H., Thorsett S. E., Arzoumanian Z., 2004, *Phys. Rev. Lett.*, 93, 141101
- Stovall K., et al., 2019, *ApJ*, 870, 74
- Tauris T. M., Savonije G. J., 1999, *A&A*, 350, 928
- Tauris T. M., Sennels T., 2000, *A&A*, 355, 236
- Tauris T. M., van den Heuvel E. P. J., 2023, *Physics of Binary Star Evolution. From Stars to X-ray Binaries and Gravitational Wave Sources*. Princeton Series in Astrophysics, Princeton University Press
- Tauris T. M., Langer N., Kramer M., 2011, *MNRAS*, 416, 2130
- Thorsett S. E., Chakrabarty D., 1999, *ApJ*, 512, 288
- Venkatraman Krishnan V., et al., 2020, *Science*, 367, 577
- Virtanen P., et al., 2019, arXiv e-prints, p. [arXiv:1907.10121](https://arxiv.org/abs/1907.10121)
- Weisberg J. M., Romani R. W., Taylor J. H., 1989, *ApJ*, 347, 1030
- Zhu W. W., et al., 2019, *ApJ*, 881, 165
- van Kerkwijk M. H., Kulkarni S. R., 1999, *ApJ*, 516, L25
- van Straten W., Demorest P., Osłowski S., 2012, *Astronomical Research and Technology*, 9, 237
- van der Velden E., 2020, *The Journal of Open Source Software*, 5, 2004
- van der Walt S., Colbert S. C., Varoquaux G., 2011, *Computing in Science and Engineering*, 13, 22

## APPENDIX A: PULSAR EPHEMERIDES

Tables of pulsar observational and derived parameters. The standard error on the last quoted digit is indicated by the values in parentheses.

## APPENDIX B: PULSAR AND COMPANION MASS MEASUREMENTS WITH THE RELEVANT REFERENCES

## APPENDIX C:

Posterior probability distributions of parameters. The figures are created using `corner.py` developed by Foreman-Mackey (2016).

This paper has been typeset from a  $\text{\LaTeX}$  file prepared by the author.

**Table A1.** Observed and derived timing model parameters for binary pulsars J0101–6422, J1101–6424, J1125–6014.

Pulsar	PSR J0101–6422	PSR J1101–6424	PSR J1125–6014
General parameters			
Reference epoch (MJD)	59130	59132	59174
MJD range	58595 – 59666	58575 – 59689	58589 – 59758
Fit $\chi^2$ / number of degrees of freedom	3018.65/3056	7574.58/7612	979.38/1027
Post-fit RMS of residuals ( $\mu$ s)	1.602	7.973	0.336
L-band observation time ( $h$ )	14.37	39.17	11.59
UHF observation time ( $h$ )	11.84	–	–
Total number of observations L-band/UHF	35/10	80/0	37/0
Spin and astrometric parameters			
Right ascension, $\alpha$ (epoch J2000; hh:mm:ss.s)	01:01:11.13637(5)	11:01:37.19156(4)	11:25:55.243407(4)
Declination, $\delta$ (epoch J2000; dd:mm:ss.s)	–64:22:30.2768(4)	–64:24:39.33311(17)	–60:14:06.81026(3)
Parallax, $\pi$ (mas)	4.5(17)	–	1.6(2)
Proper motion in RA, $\mu_\alpha \cos \delta$ (mas yr $^{-1}$ )	13.2(4)	–1.3(2)	11.07(3)
Proper motion in DEC, $\mu_\delta$ (mas yr $^{-1}$ )	–9.6(4)	–0.1(3)	–13.08(3)
Total proper motion, $\mu$ (mas yr $^{-1}$ )	16.3(5)	1.4(3)	17.13(3)
Spin period, $P$ (ms)	2.57315201365217(9)	5.10927298405781(12)	2.630380782509540(5)
First derivative of spin period, $\dot{P}$ ( $10^{-20}$ s s $^{-1}$ )	0.5083(6)	0.2591(7)	0.37303(3)
Dispersion measure, $DM$ (cm $^{-3}$ pc)	11.9217(4)	207.3647(5)	52.93371(6)
First derivative of DM, $\dot{DM}$ (cm $^{-3}$ pc s $^{-1}$ )	0.0005(5)	–0.0009(3)	–0.00105(3)
Second derivative of DM, $\ddot{DM}$ (cm $^{-3}$ pc s $^{-2}$ )	–0.0010(11)	0.0000(12)	0.00186(15)
Orbital parameters			
Orbital period, $P_b$ (d)	1.7875967338(5)	9.6117088579(9)	8.75260365059(15)
Projected semimajor axis of binary orbit, $x$ (lt-s)	1.7010463(2)	14.02463520(16)	8.33919893(3)
Time of ascending node, $T_{asc}$ (MJD)	59100.47696927(7)	59081.94129419(3)	59167.119295153(4)
First Laplace-Lagrange parameter, $\epsilon_1$ ( $10^{-6}$ )	–0.3(2)	21.57(3)	0.512(6)
Second Laplace-Lagrange parameter, $\epsilon_2$ ( $10^{-6}$ )	0.58(15)	3.94(3)	–0.612(5)
Orthometric amplitude, $h_3$ ( $\mu$ s)	0.49(11)	0.32(12)	0.84(2)
Orthometric ratio, $\zeta$	0.66(8)	0.81(15)	0.804(11)
Stochastic parameters			
Log $_{10}$ [EFAC] KAT receiver	0.008(10)	–0.010(9)	0.05(2)
Log $_{10}$ [EFAC] UHF receiver	0.030(9)	–	–
Log $_{10}$ [EQUAD] KAT receiver	–8.3(1.0)	–5.57(16)	–6.69(4)
Log $_{10}$ [EQUAD] UHF receiver	–7.9(1.2)	–	–
Log $_{10}$ [ECORR] KAT receiver	–8.5(9)	–8.5(9)	–8.4(8)
Log $_{10}$ [ECORR] UHF receiver	–8.8(8)	–	–
Log $_{10}$ [Red Amp]	–	–	–
Red Index	–	–	–
Log $_{10}$ [DM Amp]	–11.15(18)	–10.94(13)	–11.74(11)
DM Index	2.1(7)	2.8(7)	1.6(5)

**Table A2.** Observed and derived timing model parameters for binary pulsars J1514–4946, J1614–2230, J1732–5049, J1909–3744

Pulsar	PSR J1514–4946	PSR J1614–2230	PSR J1732–5049	PSR J1909–3744
General parameters				
Reference epoch (MJD)	59242	59099	59067	59059
MJD range	58834 – 59651	58589 – 59691	58526 – 59608	58526 – 59592
Fit $\chi^2$ / number of degrees of freedom	461.05/463	1673.19/1740	4437.87/4467	3523.40/2936
Post-fit RMS of residuals ( $\mu$ s)	1.487	0.648	2.300	0.090
L-band observation time ( $h$ )	11.59	7.02	18.79	23.66
UHF observation time ( $h$ )	–	–	2.84	–
Total number of observations L-band/UHF	37/0	69/0	76/5	187/0
Spin and astrometric parameters				
Right ascension, $\alpha$ (epoch J2000; hh:mm:ss.s)	15:14:19.10584(4)	16:14 : 36.50968(4)	17:32:47.766091(11)	19:09:47.424651(5)
Declination, $\delta$ (epoch J2000; dd:mm:ss.s)	–49:46:15.6363(4)	–22:30:31.539(3)	–50:49:00.3137(3)	–37:44:14.91316(19)
Parallax, $\pi$ (mas)	–	1.11(17)	0.8(6)	0.75(8)
Proper motion in RA, $\mu_\alpha \cos \delta$ (mas yr $^{-1}$ )	–7.8(2)	4.9(7)	–0.62(17)	–9.60(5)
Proper motion in DEC, $\mu_\delta$ (mas yr $^{-1}$ )	–10.3(4)	–26(4)	–9.6(4)	–35.6(2)
Total proper motion, (mas yr $^{-1}$ )	13.0(4)	27(4)	9.6(5)	36.8(3)
Spin period, $P$ (ms)	3.58933674132885(6)	3.15080765799915(4)	5.31255029615166(7)	2.947108074685310(15)
First derivative of spin period, $\dot{P}$ (10 $^{-20}$ s s $^{-1}$ )	1.8670(10)	0.9625(4)	1.4182(5)	1.4023(3)
Dispersion measure, $DM$ (cm $^{-3}$ pc)	31.00853(13)	34.48755(14)	56.82189(13)	10.39090(5)
First derivative of DM, $\dot{DM}$ (cm $^{-3}$ pc s $^{-1}$ )	–0.00016(15)	–0.00054(8)	–0.00146(16)	0.000053(12)
Second derivative of DM, $\ddot{DM}$ (cm $^{-3}$ pc s $^{-2}$ )	0.0007(5)	–0.0003(3)	0.0009(4)	–0.00020(14)
Orbital parameters				
Orbital period, $P_b$ (d)	1.9226535542(3)	8.6866194264(4)	5.2629972188(15)	1.533449477320(12)
Projected semimajor axis of binary orbit, $x$ (lt-s)	1.9332622(3)	11.29120702(7)	3.98286955(19)	1.897994789(14)
Time of ascending node, $T_{asc}$ (MJD)	59211.98535052(7)	59098.046639722(11)	59064.55306932(4)	59057.600910299(3)
First Laplace-Lagrange parameter, $\epsilon_1$ (10 $^{-6}$ )	4.0(3)	0.930(12)	1.65(9)	1.940(14)
Second Laplace-Lagrange parameter, $\epsilon_2$ (10 $^{-6}$ )	3.1(3)	–1.297(17)	–8.02(6)	–0.104(14)
Orthometric amplitude, $h_3$ ( $\mu$ s)	0.5(2)	2.340(19)	0.53(13)	0.845(7)
Orthometric ratio, $\varsigma$	0.81(13)	0.9858(3)	0.4(3)	0.9441(16)
Stochastic parameters				
Log $_{10}$ [EFAC] KAT receiver	–0.044(15)	–0.003(8)	0.008(8)	0.010(7)
Log $_{10}$ [EFAC] UHF receiver	–	–	–0.070(14)	–
Log $_{10}$ [EQUAD] KAT receiver	–8.3(1.0)	–8.6(9)	–6.00(3)	–7.75(8)
Log $_{10}$ [EQUAD] UHF receiver	–	–	–8.2(1.1)	–
Log $_{10}$ [ECORR] KAT receiver	–8.7(8)	–7.7(5)	–8.9(7)	–7.57(4)
Log $_{10}$ [ECORR] UHF receiver	–	–	–8.6(9)	–
Log $_{10}$ [Red Amp]	–	–13.3(4)	–	–13.19(15)
Red Index	–	3.9(1.3)	–	2.6(6)
Log $_{10}$ [DM Amp]	–	–11.41(11)	–11.39(9)	–11.83(9)
DM Index	–	1.4(4)	0.16(14)	1.8(3)

**Table B1.** Pulsars with estimated WD companion masses plotted in Fig 5

Pulsar	$M_p$	$M_c$	Reference
J0348+0432	$2.01^{+0.04}_{-0.04}$	$0.172^{+0.003}_{-0.003}$	Antoniadis et al. (2013)
J0437–4715	$1.44^{+0.07}_{-0.07}$	$0.224^{+0.007}_{-0.007}$	Reardon et al. (2016)
J0621+1002	$1.53^{+0.1}_{-0.1}$	$0.76^{+0.28}_{-0.07}$	Kasian (2012)
J0740+6620	$2.08^{+0.07}_{-0.07}$	$0.253^{+0.006}_{-0.005}$	Fonseca et al. (2021)
J0751+1807	$1.64^{+0.15}_{-0.15}$	$0.16^{+0.01}_{-0.01}$	Desvignes et al. (2016)
J0952–0607	$2.35^{+0.17}_{-0.17}$	$0.032^{+0.002}_{-0.002}$	Romani et al. (2022)
J0955–6150	$1.71^{+0.02}_{-0.02}$	$0.254^{+0.002}_{-0.002}$	Serylak et al. (2022)
J1012+5307	$1.72^{+0.16}_{-0.16}$	$0.165^{+0.015}_{-0.015}$	Mata Sánchez et al. (2020)
J1125–6014	$1.68^{+0.17}_{-0.15}$	$0.33^{+0.02}_{-0.02}$	This work
J1141–6545	$1.27^{+0.01}_{-0.01}$	$1.02^{+0.01}_{-0.01}$	Bhat et al. (2008)
J1614–2230	$1.94^{+0.03}_{-0.03}$	$0.495^{+0.005}_{-0.005}$	This work
J1713+0747	$1.35^{+0.07}_{-0.07}$	$0.292^{+0.011}_{-0.011}$	Arzoumanian et al. (2018)
J1738+0333	$1.47^{+0.07}_{-0.06}$	$0.181^{+0.007}_{-0.005}$	Antoniadis et al. (2012)
J1802–2124	$1.24^{+0.11}_{-0.11}$	$0.78^{+0.04}_{-0.04}$	Ferdman et al. (2010)
J1810+1744	$2.13^{+0.04}_{-0.04}$	$0.065^{+0.001}_{-0.001}$	Romani et al. (2021)
B1855+09	$1.37^{+0.13}_{-0.10}$	$0.244^{+0.014}_{-0.012}$	Arzoumanian et al. (2018)
J1909–3744	$1.45^{+0.03}_{-0.03}$	$0.205^{+0.003}_{-0.003}$	This work
J1918–0642	$1.29^{+0.1}_{-0.09}$	$0.231^{+0.010}_{-0.010}$	Arzoumanian et al. (2018)
J1933–6211	$1.42^{+0.20}_{-0.23}$	$0.422^{+0.035}_{-0.044}$	Geyer et al. 2022 (submitted)
J1946+3417	$1.828^{+0.022}_{-0.022}$	$0.2556^{+0.0019}_{-0.0019}$	Barr et al. (2017)
J1949+3106	$1.34^{+0.17}_{-0.15}$	$0.81^{+0.06}_{-0.05}$	Zhu et al. (2019)
J1950+2414	$1.496^{+0.023}_{-0.023}$	$0.2975^{+0.0046}_{-0.0038}$	Zhu et al. (2019)
J2043+1711	$1.38^{+0.12}_{-0.13}$	$0.173^{+0.010}_{-0.010}$	Arzoumanian et al. (2018)
J2045+3633	$1.251^{+0.021}_{-0.021}$	$0.873^{+0.016}_{-0.014}$	McKee et al. (2020)
J2053+4650	$1.40^{+0.21}_{-0.18}$	$0.86^{+0.07}_{-0.06}$	Berezina et al. (2017)
J2222–0137	$1.831^{+0.010}_{-0.010}$	$1.3194^{+0.0040}_{-0.0040}$	Guo et al. (2021)
J2234+0611	$1.353^{+0.014}_{-0.017}$	$0.298^{+0.015}_{-0.012}$	Stovall et al. (2019)
B2303+46	$1.34^{+0.10}_{-0.10}$	$1.30^{+0.10}_{-0.10}$	Thorsett & Chakrabarty (1999)
J2339–0533	$1.47^{+0.09}_{-0.09}$	$0.30^{+0.02}_{-0.02}$	Kandel et al. (2020)



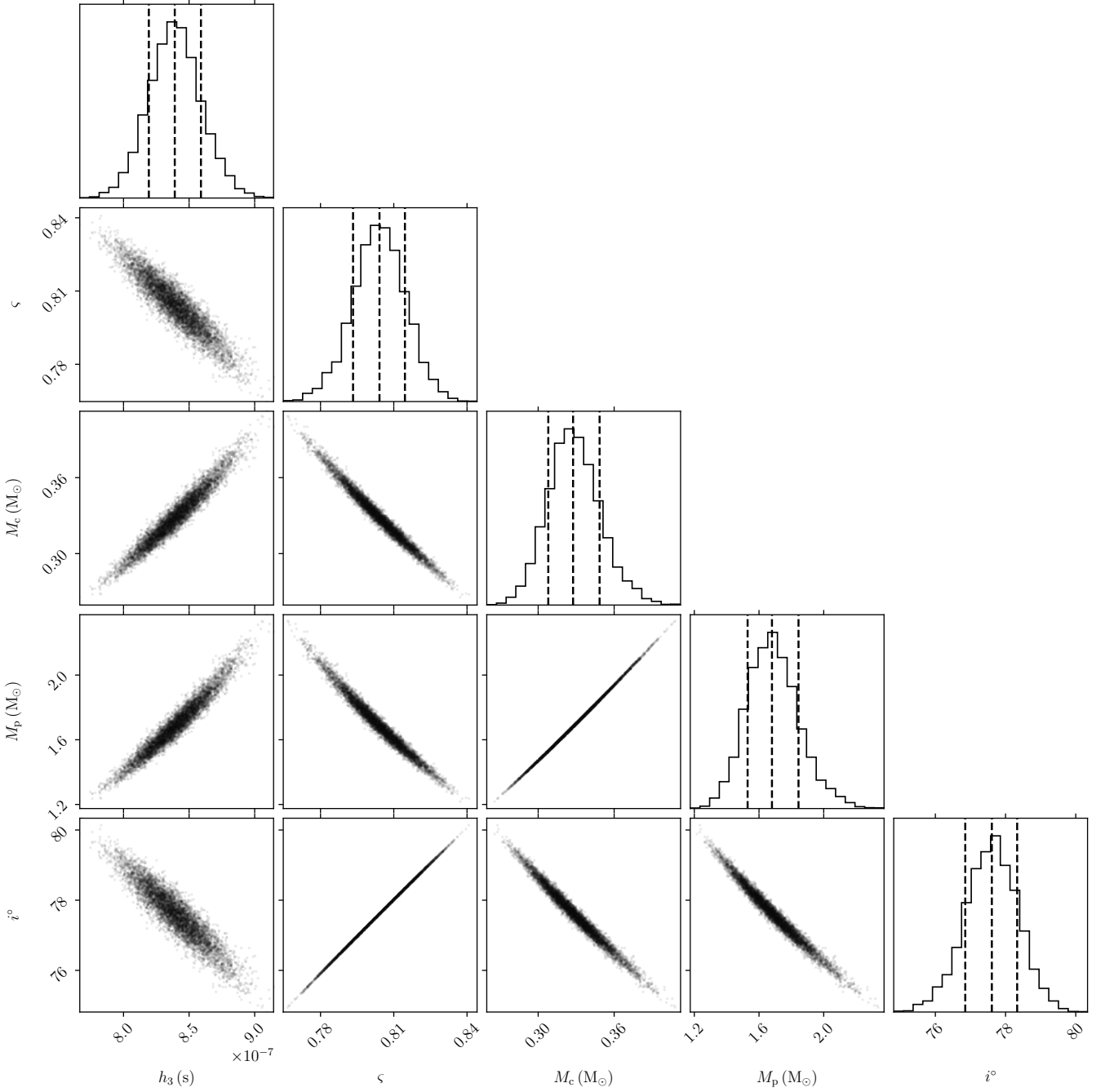


**Figure C1.** 2D marginalized posterior probability distributions of the timing parameters:  $h_3$  and  $\zeta$ , and the derived parameters:  $M_c$ ,  $M_p$ ,  $i$ , for J1125–6014. The dashed vertical lines on the 1-D histograms are showing the median and 68% confidence levels.

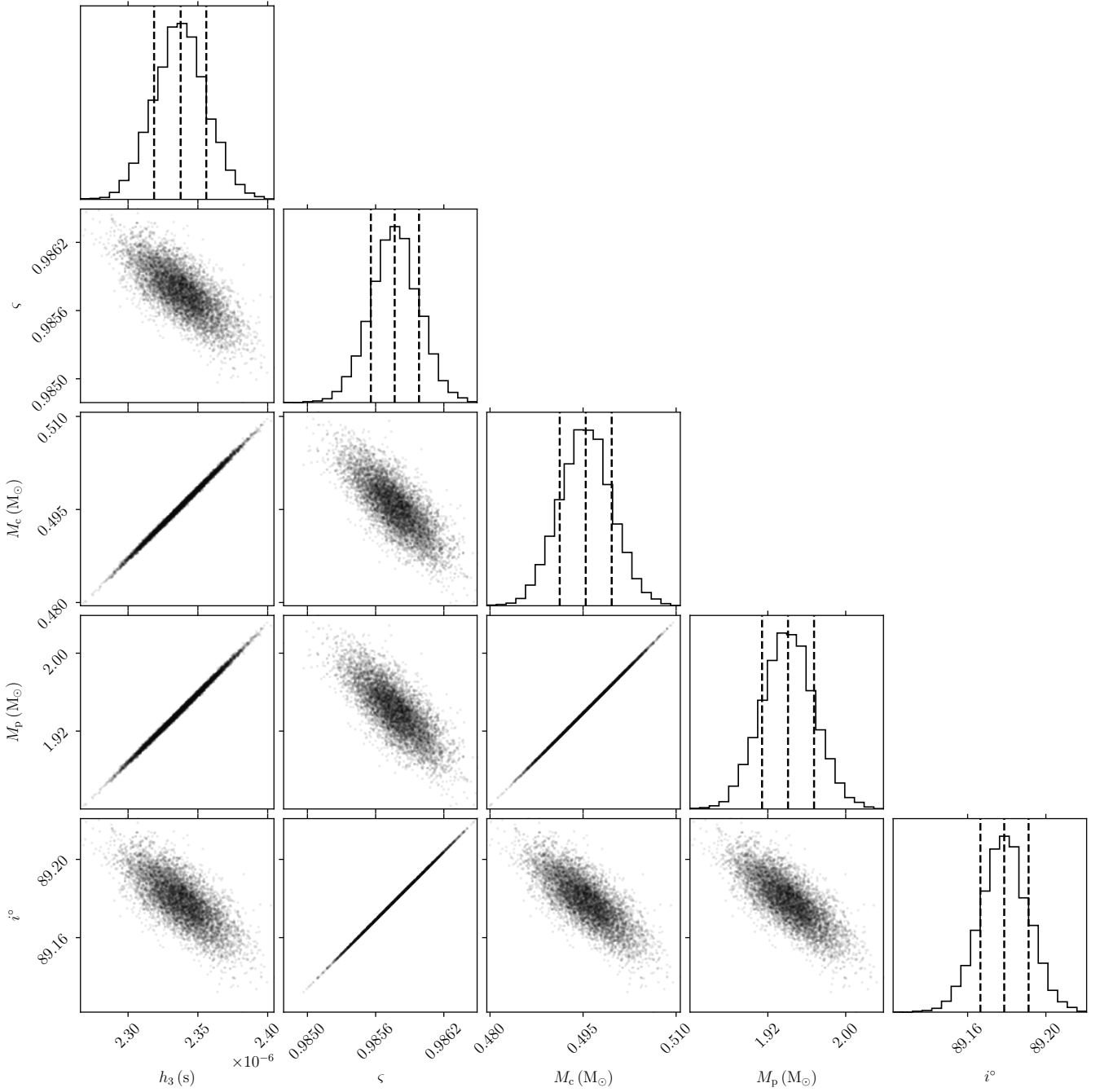


**Figure C2.** 2D marginalized posterior probability distributions of the timing parameters:  $h_3$  and  $\varsigma$ , and the derived parameters:  $M_c$ ,  $M_p$ ,  $i$ , for J1614–2230. The dashed vertical on the 1-D histograms lines are showing the median and 68% confidence levels..

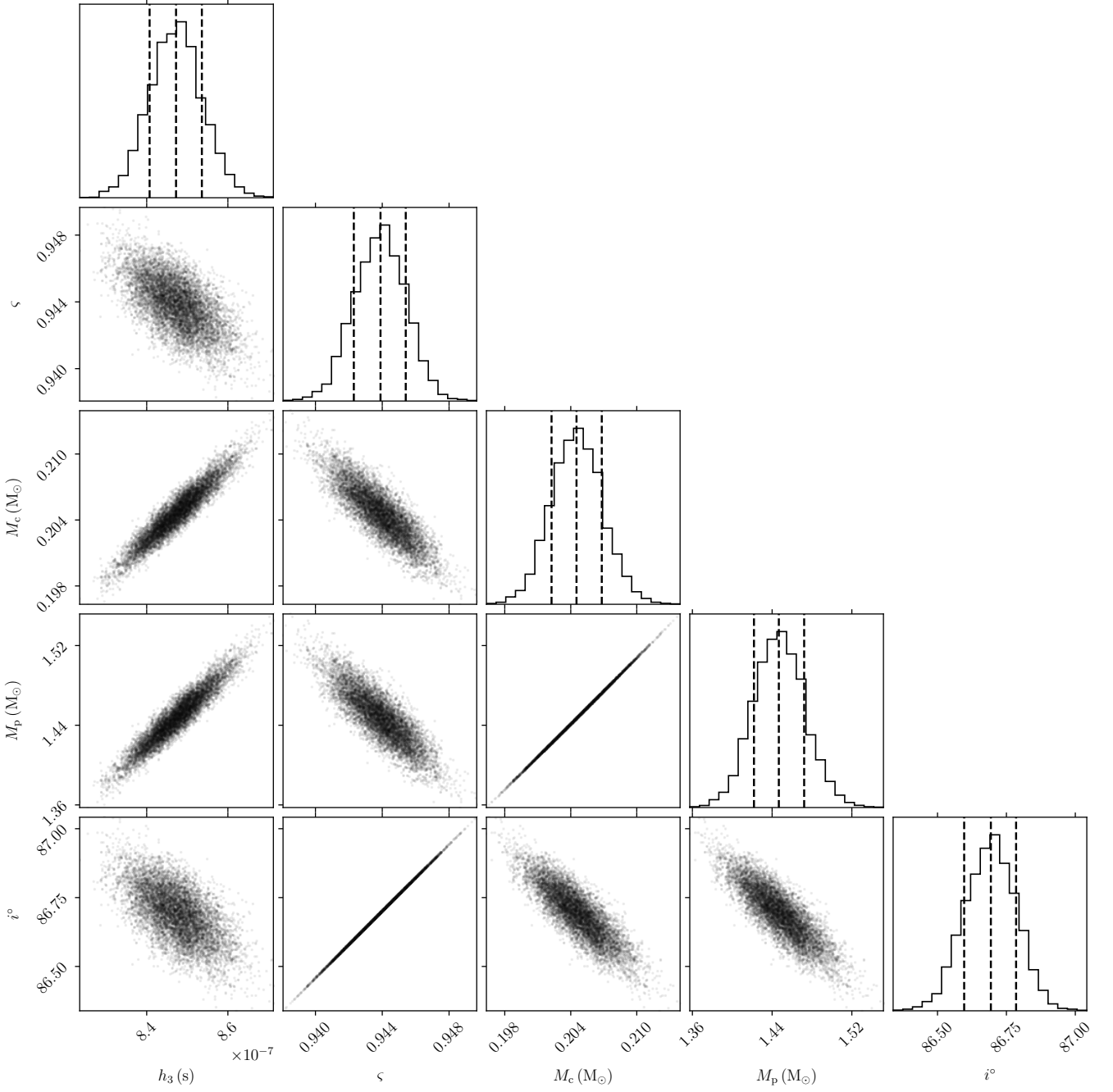


**Figure C3.** 2D marginalized posterior probability distributions of the timing parameters:  $h_3$  and  $\zeta$ , and the derived parameters:  $M_c$ ,  $M_p$ ,  $i$ , for J1909–3744. The dashed vertical lines on the 1-D histograms are showing the median and 68% confidence levels.